UNIVERSITY OF CALIFORNIA
RIVERSIDE

Interpretation of Observations from Major Air Pollution Sources Using a Variety of Dispersion Models

A Dissertation submitted in partial satisfaction
of the requirements for the degree of

Doctor of Philosophy

in

Mechanical Engineering

by

Ranga Rajan Thiruvenkatachari

March 2023

Dissertation Committee:
Dr. Akula Venkatram, Chairperson
Dr. Bhargav Rallabandi
Dr. Francesca Hopkins

The Dissertation of Ranga Rajan Thiruvenkatachari is approved:

Committee Chairperson

University of California, Riverside

AKNOWLEDGEMENTS

First, I would like to thank my supervisor Dr. Akula Venkatram, for his support and guidance throughout this journey. His vast knowledge is truly amazing, and I am grateful for all the advice and great ideas he shared with me. This dissertation would not have been possible without his tutelage. I also owe my intense research interest in this field to him.

I would like to thank Dr. Francesca Hopkins for all her help and support. Her comments challenged me and were vital in improving this dissertation. I also thank her for serving on my committee. I am grateful to David Pankratz for teaching me vital experimental skills. His level of organization and attention to detail is something I will strive for.

I would like to thank Dr. Bhargav Rallabandi for serving on my committee and for his feedback on my research. I am grateful to Dr. Marko Princevac for helping me improve my presentation skills. I would like to thank my master's mentor Dr. Shiva Nagendra for introducing me to research in air quality.

I would like to thank my colleague Yifan Ding. We have spent numerous hours working together preparing for field measurements and meetings. I would like to extend my thanks to Valerie Carranza. She helped me collect vital data used in this dissertation. I would like to thank Dr. Javier Gonzalez-Rocha for the great mentoring he provided towards the end of my Ph.D.

I would like to thank the following people for their involvement in my research: Micheal Rodriguez, Dr. Marc Fisher, Sajjan Heerah, Isis Frausto-Vicencio, Alondra Moreno, Celia Lemon and Michelle Carr.

I would like to thank my friends Irfan Ahmed, Vishnu Rajan, Suchitra Pithavath, Sanika Nishander, Shivansk Kaushik, Siddharth Arun and Bharat Kanna for their moral support at different points of this journey.

The research in this thesis was supported by the UC Lab Fees Research Program, contract number LFR-18-548581 and the California Department of Transport. The text in Chapter 2 of this dissertation is in part a reprint as it appears in Thiruvenkatachari RR, Carranza V, Ahangar F, et al (2020) Uncertainty in using dispersion models to estimate methane emissions from manure lagoons in dairies. Agric For Meteorol 290:108011. https://doi.org/10.1016/j.agrformet.2020.108011. The text in Chapter 3 of this dissertation is in part a reprint as it appears in Thiruvenkatachari RR, Ding Y, Pankratz D, Venkatram A (2021) A field study to estimate the impact of noise barriers on mitigation of near road air pollution. Air Qual Atmos Heal. https://doi.org/10.1007/s11869-021-01104-9.

Finally, I would like to thank my parents Thiruvenkatachari and Jayanthi for their belief, encouragement, and patience. I owe everything to them.

ABSTRACT OF THE DISSERTATION

Interpretation of Observations from Major Air Pollution Sources Using a Variety of Dispersion Models

by

Ranga Rajan Thiruvenkatachari

Doctor of Philosophy, Graduate Program in Mechanical Engineering
University of California, Riverside, March 2023
Dr. Akula Venkatram, Chairperson

This dissertation summarizes the results from the development and application of models to investigate the transport and dispersion of pollutants from two major sources. In the first study, I formulate and apply a dispersion model to estimate emissions of methane from manure dairy lagoons, In the second, I examine the role of noise barriers in mitigating the impact of vehicular emissions on near-road air quality. I also present the development and application of a semi-empirical meteorological model to compute meteorological inputs required by dispersion models using measurements from instruments that are simpler and less cumbersome than those being used now.

Manure lagoons in dairies make significant contributions to emissions of methane, a major greenhouse gas. Because there is no direct method to estimate these emissions, a variety of methods have been developed to infer these emissions from concentration measurements made close to lagoons. My research involves developing such an inference approach based on a state-of-the-art dispersion model combined with a unique sampling strategy. My

approach also allows for estimating the uncertainty in these emission estimates. I demonstrate my approach by applying it to estimating methane emissions from two manure lagoons, one located in southern California and the other in northern California. I compare my results with those obtained from a popular approach based on a Lagrangian particle dispersion model.

Air pollution associated with vehicle emissions from roadways has been linked to a variety of adverse health effects on people living within 100 m of roadways. Wind tunnel and tracer studies indicate that near-road noise barriers have a mitigating impact on air pollution caused by vehicular emissions. Data from these studies formed the basis of a barrier model that accounted for this mitigating effect. This model has been incorporated into a research version of AERMOD, a model recommended by the USEPA for estimating the impact of a variety of pollution sources including highways. Before AERMOD can be used for regulatory applications that give credit for the mitigating effect of noise barriers, the barrier component of the model must be evaluated with real-world data with its attendant complexities that were absent in the controlled wind tunnel and tracer studies. I made significant contributions to the design and conduct of a comprehensive field study that UCR conducted to collect the data required to evaluate the performance of the barrier component of AERMOD. An analysis of the data indicates that AERMOD is likely to underestimate mitigation from barriers at low wind speeds. We suggest an approach to correct this problem.

Currently used dispersion models require meteorological inputs that are best computed with time-resolved velocity and temperature measurements made with 3-D sonic

anemometers. Because such measurements are not routinely available, there is a need for methods that provide accurate estimates of these inputs using equipment that is easy to set up and provides measurements that can be readily interpreted. I demonstrate such a method based on measurements of horizontal wind speeds and temperature fluctuations. The method is evaluated by comparing methane emissions from a dairy manure lagoon inferred from a dispersion model that uses modeled meteorological inputs to those from measurements with a 3-D sonic anemometer. We show that this method can be adapted for temperature fluctuations measured with a low-cost temperature sensor that is unable to resolve the high-frequency temperature fluctuations captured by sonic anemometers.

Table of Contents

List of Figures

List of Tables

1 Introduction and Objectives

1.1 Background

Atmospheric dispersion models are mathematical descriptions of the atmospheric processes that govern the transport, dispersion, removal, and chemical transformation of pollutants emitted by sources (Venkatram and Schulte 2018a). Once the results from a dispersion model have been evaluated with measurements, the model can be used as a surrogate for reality to conduct numerical experiments that are difficult or impossible to conduct. For example, atmospheric dispersion models can be used to estimate pollutant concentrations where measurements are not available (Pineda Rojas 2014; Ahangar et al. 2019). This is especially important for regulatory purposes where the impact of planned or existing pollutant sources needs to be determined at various locations. Thus, dispersion models are important in ensuring that air quality in a region is acceptable.

Sometimes direct measurements of emission rates of pollutants from sources such as manure lagoons, wind-blown dust from dried up lake beds, are not possible. In such cases it is necessary to infer emission rates from measurements of pollutant concentration around these sources. In such cases, dispersion models can be applied to infer the emission rate by fitting these measurements to model estimates treating the emission rate as the unknown parameter. This

technique of inferring emissions rates from the measured pollutant concentration using a dispersion model is called Inverse Dispersion Modelling (Kia et al. 2022; Bühler et al. 2022).

A dispersion model accounts for pollutant transport by, dispersion due to turbulence, scavenging due to dry and wet deposition, and chemical transformations (Venkatram and Schulte 2018a). The time scales of these processes relative to the transport time scale between the source and receptor determine the relative importance of the processes. Continuous pollutant emissions with source-receptor distances of the order of tens of kilometers are modelled as continuous plumes governed by meteorology near the source, when scavenging and chemical transformation are slow relative to the transport time scale. Some popular models using this approach are AERMOD (Cimorelli et al. 2005), RLINE (Snyder et al. 2013) and OML (Olesen et al. 2007)

When the source-receptor distance becomes large, the wind fields between the source and receptor will show variations in both space and time. In such cases puff models or Eulerian grid models are usually used. In a puff or a particle model, a puff or air parcel consisting of the emissions from the pollutant source over a short period of time is tracked from the source through the varying wind fields. The puff evolves in response to the wind fields, turbulence, chemistry and scavenging of the species as it is transported from source to receptor. A puff model is resource intensive because it is necessary to release and track a large number of puffs to construct a time-averaged concentration at a receptor. The computational needs of a puff model can be reduced by applying a receptor-oriented approach. In this approach, the concentration at a receptor is only affected by the puffs that reach the receptor in the time of interest. The history of the puff before it reaches the receptor is calculated to determine the impact of the puff at the receptor. Some of the models using this approach are WindTrax (Flesch et al. 1995) and CALPUFF (Scire et al. 1990).

Eulerian grid models involve solving the mass conservation equation using a grid of boxes. A mass balance is performed in each box of the grid over a time interval that is small compared to the time scale of variation of the dominant governing processes. Inflow and outflow due to transport and turbulence, dry and wet deposition, and chemical transformation occurring within each box are considered in the mass balance. Each box in the grid is interconnected with each other such that the outflow from one box is the inflow into the adjacent box. The computational demand of a grid model is proportional to the number of grid boxes used in the model. Thus, it is often impractical to resolve plumes from sources individually in a grid model. Grid-based models are the best framework for straightforward treatment of chemical processes; each grid box is treated as a well-mixed reactor. CMAQ (Appel et al. 2021) and WRF-CHEM (Grell et al. 2005) are dispersion models that treat chemistry using Eulerian grids.

This dissertation focuses on the development and application of dispersion models for short range transport to investigate surface releases from major air pollution sources. These models are applicable for source-receptor distances in the order of a kilometer. At these short distances the major processes that govern the fate of the pollutant are transport due to mean winds and turbulent dispersion. Thus, the transport is modelled as continuous plumes with the meteorology assumed to be homogeneous in space and time.

1.2 Objectives

My research focuses on the development and application of dispersion models at scales of tens of meters between source and receptor. At these distances the major processes that govern the fate of the pollutant are transport by mean winds and turbulent dispersion. The meteorology is assumed to be homogeneous in space in these models.

In this thesis, I report on the development and application of dispersion models to address two problems:

1. Estimation of methane emissions, an important greenhouse gas, from manure lagoons located in dairies. I pay particular attention to quantifying the uncertainty associated with emission estimates.

2. Evaluation of dispersion models designed to estimate the impact of vehicle-related pollutant emissions on air quality next to roads. These models incorporate algorithms to account for the mitigating effect of near-road noise barriers on near-road air quality. I played a major role in conducting field studies to collect the data required to perform this evaluation and developed a method to estimate the inputs required by dispersion models using relatively simple measurements of scalar variables.

1.3 Structure of the dissertation

Chapter 2 describes the field experiments and the modelling techniques used to infer the CH_4 emissions and their uncertainties from dairy manure lagoons. Chapter 3 describes a field study to collect data required to evaluate and improve a dispersion model that accounts for the impact of noise barriers on near-road air quality; the field study involved release of a tracer from vehicles traveling on a highway with a roadside noise barrier, collection of the tracer using automated samplers, and analysis of the sampled gases in the laboratory. This chapter also describes the evaluation of a semi-empirical dispersion model using data from the field study. I also suggest modification of the model to reduce the discrepancies between model estimates and corresponding measurements when the wind speeds are low. Chapter 4 describes the formulation of a model that estimates the

meteorological parameters required by dispersion models without measurements with a 3-D sonic anemometer. The model uses measurements of horizontal wind speeds and temperature fluctuations, which facilitates on-site measurements of micrometeorological inputs with mobile platforms. Finally, Chapter 5 lists the major conclusions from each of these studies.

2 Estimating Methane Emissions from Dairy Manure Lagoons using Dispersion Models

2.1 Introduction

Atmospheric concentrations of methane (CH_4), an important greenhouse gas, have tripled since the industrial revolution (Yu et al. 2018). Methane has an important role in causing climate change, with emissions rising more quickly than those of CO_2 (Saunois et al. 2016b). CH_4 is ten times more potent than CO_2 in warming the atmosphere. Given the short lifetime and the potential for rapid mitigation, controlling CH_4 emissions has become a priority for achieving short-term climate goals (United Nations, 2021).

Animal agriculture is the source of ~35% of anthropogenic methane emissions globally, and these emissions are increasing along with the number of animals (Saunois et al. 2016a). Methane emissions from animal agriculture derive primarily from enteric fermentation in cattle and from manure management, particularly when waste is treated or stored in anaerobic lagoons. Manure management accounts for nearly 10% of methane emissions in the U.S. (US Environmental Protection Agency 1990), and in California, more than a quarter (CARB 2019). However, as pointed out by a report from the National Academies of Sciences, Engineering 2018, these inventories are not supported adequately by

measurements. Furthermore, the report concludes that "fundamental research identifying and quantifying uncertainties is needed".

Currently, the US Environmental Protection Agency (US EPA) and California Air Resources Board (CARB) rely on a bottom-up estimate formulated by Mangino et al., (2002) to estimate the CH_4 emissions from manure lagoons in their emission inventories. There have been studies that show that the bottom-up estimates might underpredict CH_4 emissions (Baldé et al. 2016; Hristov et al. 2017). Thus, there is a need to fill in key gaps in our understanding of the variability of methane emissions from manure lagoons in dairy farms. The methane emission rates inferred from the manure lagoons by applying dispersion models could be used to refine the empirical formulations of the bottom-up estimates, which are applied to obtain state-wide or nation-wide emission inventories.

2.2 Background and Approach

Methane emissions from area sources, such as manure lagoons, have been inferred using several micrometeorological methods, which are critically reviewed in McGinn, (2013). This work focuses on one of these methods, based on using dispersion models, to infer emissions from measurements of the concentrations of the relevant species near the source. Dispersion models have been used by several investigators (Ro et al., 2013; Leytem et al., 2017) to estimate emissions from lagoons and determine their uncertainty. Most have used the WindTrax software, based on the backward Lagrangian particle model developed by Flesch et al. (2005), to infer emissions from path-averaged methane concentrations measured upwind and downwind of the lagoon of interest. Some of these studies have

quantified the uncertainty in these emissions. Kaharabata et al., (2000) used the approximate solution of the two-dimensional diffusion equation proposed by van Ulden, (1978) to infer emission rates from a 4 by 8 m plot with a tracer gas with a known release rate. 81% of the measurements made near the centerline of the plumes yielded emission estimates within ±20% of the actual source strength and within 22% to 55% away from the centerline. Ro et al. (2013) estimated the uncertainty using a similar approach. The inferred emission estimate was within a range of 0.68 to 1.08 of the actual value. Determining emission uncertainty using tracer releases is the most direct approach. However, a tracer study is not practical for typical lagoons with lengths and widths of the order of 100 m, and the results would be difficult to transfer to conditions that differ from those of the tracer study.

In this study, we apply two dispersion models to estimate methane emissions from waste lagoons in two dairies, one located in Southern California, and the other in Central California. The difference in the results from the two models is one measure of the uncertainty in inferring emissions using dispersion models.

Our application of dispersion models to infer emission rates of methane differs from others in several ways. The first is that the Eulerian model is a numerical solution of the mass conservation equation to model the vertical distribution of concentrations; the eddy diffusivity is specified using Monin-Obukhov similarity theory. Nieuwstadt and van Ulden, (1978) show that the solution agrees remarkably well with observations at the surface as well as of the vertical distribution of concentrations measured during the Prairie Grass experiment (Barad 1958). Thus, we do not have to resort to the often-used Gaussian

distribution, which is a useful approximation only under very stable conditions. The numerical solution also avoids specifying the height at which the plume is transported, which is usually chosen arbitrarily or needs to be computed from an implicit equation (van Ulden 1978). We refer to this model as the Eulerian Numerical (EN) model.

Lagrangian particle methods offer similar advantages and have been used by several investigators (Todd et al., 2011; Ro et al., 2013; Grant et al., 2013; Baldé et al., 2016; Leytem et al., 2017). The model used in this study is that formulated by Flesch et al., (2005) and converted into free software called WindTrax (http://www.thunderbeachscientific.com/). This model, which computes emissions by tracking particles from the receptor to the source in a turbulent flow field, belongs to a class of models referred to as backward Lagrangian Stochastic (bLS) models. Details of the model can be found in the cited paper.

The second way that this study differs from previous studies is the strategy used to sample atmospheric methane concentrations, which allows us to provide indirect estimates of the uncertainty in the inferred emissions associated with the uncertainty in the model physics. Our approach is to station the measurement platform at several locations around the lagoon to make time-averaged measurements of atmospheric methane accompanied by simultaneous measurements of micrometeorology. These measurements are then fitted to estimates from dispersion models that use the corresponding micrometeorological inputs to yield the unknown emission estimates. The residuals between model estimates and corresponding measurements are used to estimate the 95% confidence intervals of the inferred emission rates.

The technique shown here can be used across multiple times of days and seasons to examine the role of temporal drivers of emissions from similar area sources. This technique also has the following advantages over previous studies: (1) it is easily deployable and applicable to other gases if they are measured, (2) it enables separate emission estimates for different sectors of the manure management system, (3) it provides uncertainty estimates for emissions, and (4) it does not require a measurement of background methane concentrations as the background is a parameter fitted in the model.

2.3 Methodology

Measurements were made near the manure lagoons in two dairies using a mobile platform that circulated around the lagoon complex and a stationary meteorological tower. Atmospheric methane (CH_4) mixing ratios were collected with a cavity ring-down spectrometer (Picarro 2210-i) in the mobile platform, a Mercedes Sprinter van. An inlet was located at the front of the vehicle's roof 2.87 m above ground level through which the outside air was pumped and sampled approximately every second by the analyzer. A GPS receiver (Garmin GPS 16X) mounted on the vehicle's roof was used to collect high-precision geolocation data. Data from the CH_4 analyzer was calibrated against standards tied to the NOAA scale measured before and after data collection following Hopkins et al., 2016. The general sampling approach was to drive the mobile platform around the lagoon complex, stopping for ~10-minute intervals to collect atmospheric CH_4 mixing ratios at 29-42 receptor locations around the perimeter.

The meteorological inputs to the model were collected using a 3-D Sonic Anemometer (CSAT3, Campbell Scientific) mounted on a stationary tower located on the dairy farm within 500 m of the most distant receptor location sampled by the mobile platform. At Southern California dairy, measurements were made at a height of 2.6 m and a frequency of 10 Hz. At the Central California dairy, measurements were made at a height of 2.4 m and a frequency of 20 Hz.

The dispersion models are used to estimate emissions through the relationship that relates the measured atmospheric methane concentration (mixing ratio) at any receptor $'j'$ to the corresponding model estimate

$$C_j = C_b + \sum_i E_i T_{ij} + \varepsilon_j \tag{2.1}$$

where T_{ij} is the modeled impact of source $'i'$ on receptor $'j'$ using a unit emission rate, E_i is the unknown emission rate from source $'i'$, and ε_j is the residual. The background concentration, C_b is also treated as an unknown. The emissions and the background concentrations are the values that minimize $\sum_j \varepsilon_j^2$ with the constraint that their values are greater than or equal to zero. To achieve this, we use the MATLAB function *lsqnonneg* described in Lawson and Hanson 1974, Chapter 23, p. 16.

The 95% confidence intervals for these emission rates and background concentration are computed through a version of bootstrapping: the difference between the residuals ε_j and the mean residual $< \varepsilon_j >$ are added randomly to the best fit model estimates to create 1000 sets of pseudo-observations, which are then fitted to the model estimates to create sets of

emission rates and background concentrations. The 95% confidence interval corresponds to the 2.5 and the 97.5 percentiles of these sets.

2.4 Dispersion Model

In the model, the manure lagoon is represented as a set of area sources. In the EN model, the contribution of each area source to the concentration at a receptor at (x_r, y_r, z_r) is an integral over a set of line sources perpendicular to the wind direction. As shown in Figure 2-1, each line source spans the area source and is placed perpendicular to the near surface wind speed; the x-axis of the co-ordinate system is parallel to the direction of the surface wind speed. This allows us to compute the contribution of each line source to the concentration at the receptor using the expression (Venkatram and Horst 2006)

$$C(x_r, y_r, z_r) = qF_z(x_r - x_l, z_r)\left(erf(t_2) - erf(t_1)\right)/2, \tag{2.2}$$

where q is the emission rate per unit length of line source, x_r, y_r, z_r, are the co-ordinates of the receptor, x_l is the x-co-ordinate of the line source, $F_z(x, z)$ is the cross-wind integrated vertical distribution of the concentration, and

$$t_i = \frac{y_{li} - y_r}{\sqrt{2}\sigma_y(x_r - x_l)}. \tag{2.3}$$

The number of line sources used to compute the integral is successively doubled until the absolute relative difference between successive integrals, extrapolated to zero distance between lines, is less than 10^{-4}.

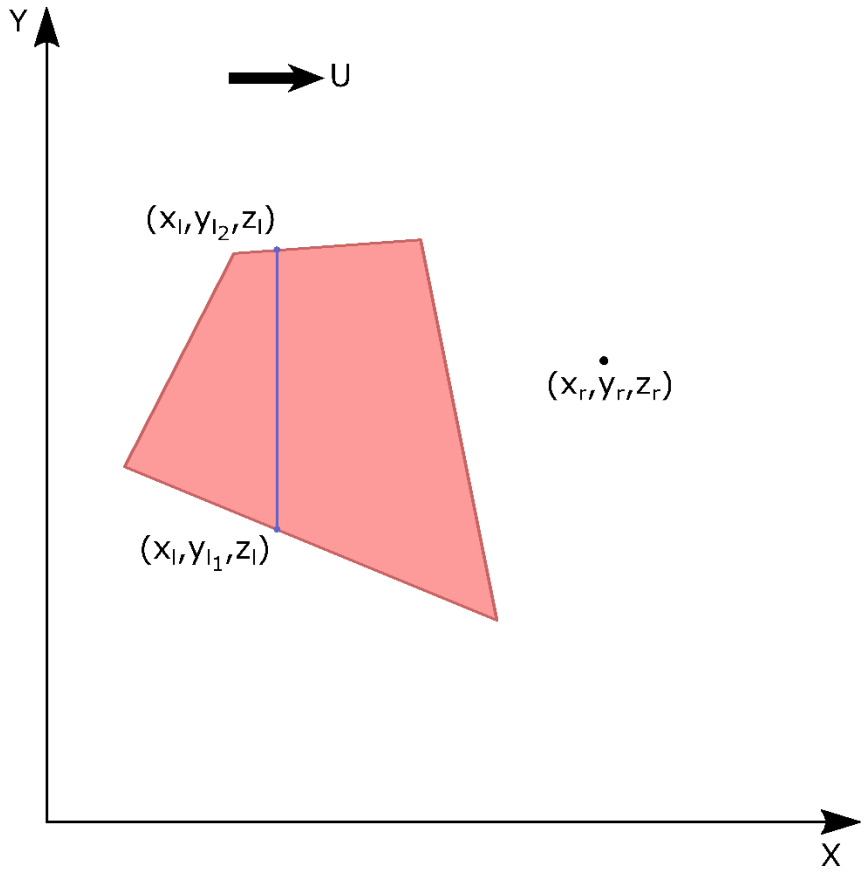

Figure 2-1 The red polygon represents the area source. The blue line represents a single line source perpendicular to the wind speed ($\boldsymbol{U}$). The receptor is at ($\boldsymbol{x_r, y_r, z_r}$).

The vertical distribution of concentrations, $F_z(x, z)$ is the numerical solution of the two-dimensional mass conservation equation. Nieuwstadt and van Ulden (1978) showed that the solution of the mass conservation provides an excellent description of the cross-wind integrated concentrations measured during the Prairie Grass Experiment (Barad 1958) if the wind speed, $U(z)$ and the eddy diffusivity, $K(z)$ are expressed using Similarity Theory relationships (Businger et al. 1971).

The two-dimensional mass conservation equation is

$$U(z)\frac{\partial F_z}{\partial x} = \frac{\partial}{\partial z}\left(K(z)\frac{\partial F_z}{\partial z} \right)$$
$$\textit{and} \qquad (2.4)$$
$$Q = \delta(z = z_s) \;\; \textit{at } x=0$$

where $K(z)$ is the vertical eddy diffusivity, and $U(z)$ is the horizontal velocity. The emission at $x = 0$ is specified by assigning non-zero concentrations to three vertical levels: at $z = z_s$ and two heights below and above $z = z_s$. The results of the numerical solution of Equation (2.4) are normalized by the integral $\int_0^H U(z)F_z(x,z)dz$, the horizontal mass flux at x close to the source to obtain the solution for unit emission rate. Where H is the top of the modeling domain.

The mass conservation (Equation (2.4)) models turbulent dispersion using the concept of eddy diffusivity, which can be justified only when the travel time from the source is much larger the relevant Lagrangian time scale that governs particle motion in the turbulent flow (Mooney and Wilson 1993); its success in describing dispersion from surface releases provides posteriori justification for its use.

The boundary conditions for the solution of Equation (2.4) are

$$K(z)\frac{\partial F_z}{\partial z} = -v_d F_z \;\; \textit{at } z=z_o$$
$$\textit{and} \qquad (2.5)$$
$$\frac{\partial F_z}{\partial z} = 0 \;\; \textit{at } z=H$$

where v_d is the deposition velocity, taken to be zero for methane, and z_0 is the roughness length.

The horizontal plume spread, σ_y, used in the Equation (2.3), for the contribution of a line source is based on the expression suggested by Eckman (1994) and applied by Venkatram et al., (2013) to describe horizontal spread of plumes released during the Prairie Grass field study:

$$\frac{d\sigma_y}{dx} = \frac{\sigma_v}{U(\bar{z})}$$

where $\bar{z}$, the center of mass of the vertical distribution is (2.6)

$$\bar{z} = \frac{\int_0^\infty C(z)zdz}{\int_0^\infty C(z)dz}$$

The horizontal domain for the solution of Equation (2.4) is taken to be 1.2 times the maximum distance between the vertex of the area source and the receptors. The vertical domain is taken to be 400 m, which is several times larger than the vertical spread of the plume at the maximum source-receptor distance of a few hundred meters. The horizontal grid points are linearly spaced with a distance between points of about 5 m, and the vertical spacing is logarithmic with 400 points to provide fine resolution close to the surface. The concentrations at receptors that do not coincide with grid points are computed using two-dimensional linear interpolation.

The backward-Lagrangian stochastic model used in this study was formulated by Flesch et al., (2005). The model releases particles from a receptor and traces their path backward in time in a turbulent flow field until they leave the domain that includes the source. The

source receptor matrix connecting the source at $'i'$ to the receptor at $'j'$ is given by the deceptively simple expression

$$T_{ij} = \frac{1}{N_j} \sum_{k=1}^{k=P_{ji}} \left| \frac{2}{w_{ji}^k} \right| \frac{1}{A_i} \tag{2.7}$$

where N_j $(= 50{,}000)$ is the number of particles released from the receptor, j and w_{ji}^k is the vertical velocity of the k^{th} particle released from the receptor, j that touches down on the source, i, with an area A_i. The number of particles that touch down on the source, i from the receptor, j, $P_{ji} \leq N_j$, because only a fraction, P_{ji}/N_j of the released particles impact the source. The model has been converted by Thunder Beach Scientific into software called WindTrax, which is widely used to estimate emissions from small area sources.

2.5 Results

We evaluate the performance of the models in this study using the following statistics: the coefficient of determination (R^2) between model estimates and corresponding measurements, the percentage of predicted concentrations within a factor of 2 of the observed concentration ($fact2$), the geometric mean (m_g) and the geometric standard deviation (s_g) of the residuals between model estimates and observations. The m_g and s_g are computed using the following equations,

$$\begin{aligned} \varepsilon_m &= \ln\ C_p\ - \ln\ C_o \\ m_g &= \exp(\langle \varepsilon_m \rangle) \\ s_g &= \exp\ \sigma\ \varepsilon_m \end{aligned} \tag{2.8}$$

where C_p and C_o are the model estimate and measured concentrations respectively, $\langle \quad \rangle$ represents average and σ represents standard deviation. The deviation of m_g from unity indicates the model bias with values greater than one indicating overprediction and values less than one indicating underprediction; s_g represents the uncertainty in the model with s_g^2 approximately representing the 95% confidence interval of the ratio, C_p/C_o.

2.5.1 Southern California Dairy

The Southern California dairy consists of five manure lagoon ponds shown in Figure 2-2(a). The liquid manure stream enters the right-most pond shown in the left panel of Figure 2-2(a), outlined in red, and flows sequentially by gravity through the remaining ponds to the left indicated by red arrows. Initially the mobile platform circulated around the whole lagoon complex. Preliminary modeling indicated that the red highlighted lagoon in Figure 2-2(a) contributed more than 90% to the total methane emissions, consistent with the expectation that the highest emissions should come from the lagoon with the greatest amount of volatile solids (fresh manure). Subsequent measurements and modeling focused on quantifying emissions from just this lagoon. To capture heterogeneity in emissions across the surface of this lagoon, we divided the lagoon into four area sources and each one modeled separately as shown in Figure 2-2(b).

The mobile platform stopped at each of the marked receptors for about 10 to 15 minutes during the course of about 4 hours of observations on August 08th, 2018. Simultaneous micrometeorological measurements were made with a 3-D sonic anemometer located to

the left of the highlighted lagoon as shown on Figure 2-2(b). Table 2-1 summarizes the meteorological conditions and the measurement periods.


Google Earth
N
200 m

(a)

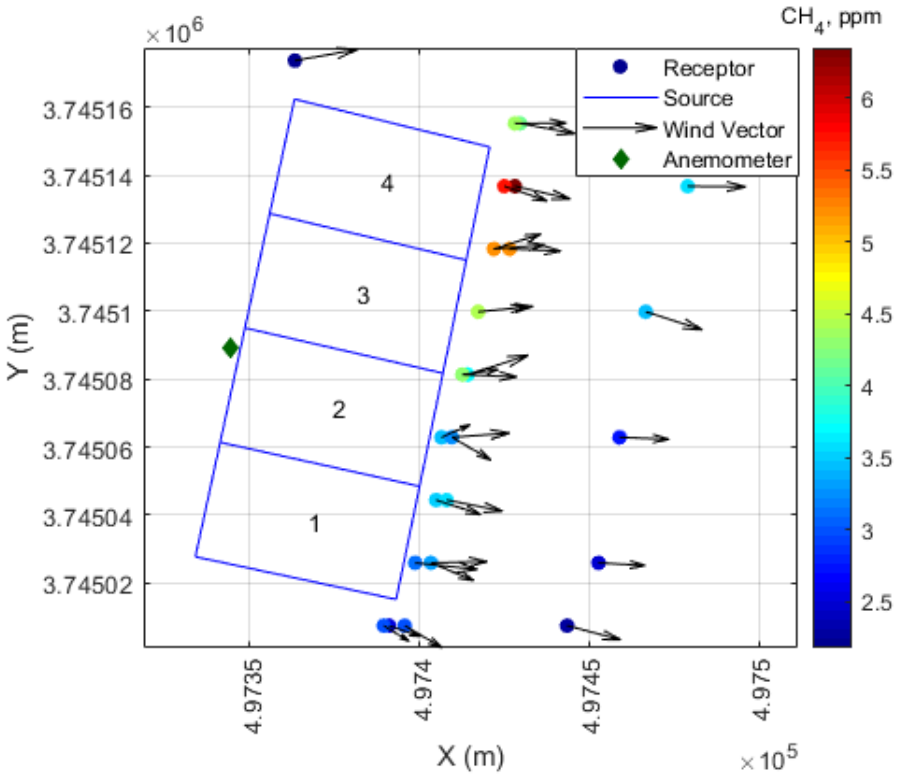
×10^6
3.74516
3.74514
3.74512
3.7451
3.74508
3.74506
3.74504
3.74502
Y (m)
4.9735
4.974
4.9745
4.975
X (m)
×10^5
CH4, ppm
6
5.5
5
4.5
4
3.5
3
2.5
Receptor
Source
Wind Vector
Anemometer
1
2
3
4

(b)

Figure 2-2 (a) An aerial value of the manure lagoon complex at the Southern California dairy. Red arrows show the flow of the manure. (b) Model setup showing the source, the receptors as circles, color coded by concentration and the wind vector represented as black arrows.

Table 2-1 Details of sampling times, concentrations and associated meteorological parameters during the measurement period

Receptor #	Start Time (hrs)	End Time (hrs)	Concentration (ppm)	Wind Speed (m/s)	σ_w (m/s)	Wind Direction (Deg)	u_* (m/s)	MO Length (m)
	08/14/2018							
1	10:52	11:06	2.53	2.3	0.23	309	0.16	-10.9
2	11:13	11:24	2.98	2.1	0.20	322	0.10	-3.4
3	11:25	11:36	2.99	3.1	0.25	321	0.13	-6.0
4	11:37	11:47	3.20	3.3	0.29	312	0.31	-61.7
5	11:48	11:58	3.49	3.3	0.30	308	0.20	-12.8
6	11:59	12:09	3.42	2.2	0.28	266	0.27	-57.7
7	12:10	12:20	4.04	3.2	0.27	320	0.21	-17.3
8	12:21	12:31	3.92	2.5	0.27	282	0.20	-26.2
9	12:32	12:42	4.30	3.4	0.32	284	0.23	-27.9
10	12:44	12:57	4.59	3.5	0.28	272	0.06	-0.6
11	12:58	13:10	5.18	3.6	0.30	292	0.18	-15.1
12	13:12	13:24	6.35	4.0	0.31	303	0.32	-63.3
13	13:28	13:38	4.14	3.9	0.30	301	0.22	-20.5
14	14:20	14:25	2.18	4.5	0.34	280	0.22	-21.1
15	14:26	14:31	4.34	3.6	0.32	290	0.15	-6.8
16	14:31	14:36	5.75	3.2	0.25	309	0.22	-36.9
17	14:37	14:42	5.22	3.6	0.33	285	0.29	-42.8
18	14:42	14:47	4.45	3.9	0.32	284	0.17	-11.4

19	14:47	14:52	3.71	4.5	0.37	272	0.21	-11.1
20	14:53	14:58	4.28	3.9	0.31	293	0.25	-38.0
21	14:58	15:03	3.26	4.1	0.35	286	0.26	-26.4
22	15:04	15:09	3.58	4.0	0.33	301	0.23	-49.8
23	15:09	15:14	3.34	4.0	0.32	289	0.18	-8.6
24	15:15	15:20	3.13	4.4	0.31	296	0.26	-45.8
25	15:20	15:25	2.31	3.9	0.34	305	0.19	-13.8
26	15:26	15:32	2.45	3.3	0.26	293	0.18	-25.8
27	15:33	15:39	2.76	3.5	0.25	292	0.25	-56.7
28	15:41	15:47	3.45	4.2	0.30	308	0.20	-34.1
29	15:59	16:11	3.56	4.1	0.33	291	0.20	-19.9

The results of the modeling exercise are presented in Figure 2-2 and Table 2. The area sources correspond to the bottom panel of Figure 1, where the primary lagoon marked in red is divided into 4 smaller regions numbered 1 to 4.

Figure 2-3(b) and Figure 2-4(b) show the scatter plot between the predicted and measured CH_4 concentration from the EN and bLS model respectively. The R^2 between model estimates and the corresponding measurements is 0.86 for the EN model (Figure 2-3(b)) while it is 0.85 for the bLS model (Figure 2-4(b)). Geometric means, m_g, of 1.01 for the EN model and 0.93 for the bLS model indicate that there is little bias in the models. All the predicted values lie with a factor of 2 of the observed values for both the models. Geometric standard deviations, s_g, of 1.10 and 1.13 for the EN and bLS model respectively indicate little spread in the estimated concentrations. Both the models are able to predict the highs and lows in the observed CH_4 concentrations very well (Figure 2-3(a); Figure 2-4(a)).

Table 2-2 tabulates the emission rates inferred from the models. The estimate of total emission from the lagoon is 386 kg/d from the EN model, which is 1.83 times the bLS model estimate of 211 kg/d; there are also differences in the emissions rates inferred from the two models for the four sources. The uncertainty in the inferred emission rates is characterized by the 95% confidence interval, the limits of which are normalized by best fit value. Source 4, where the inlet for the manure stream is located, has the largest contribution to the total emissions and the smallest uncertainty range (Table 2-2).

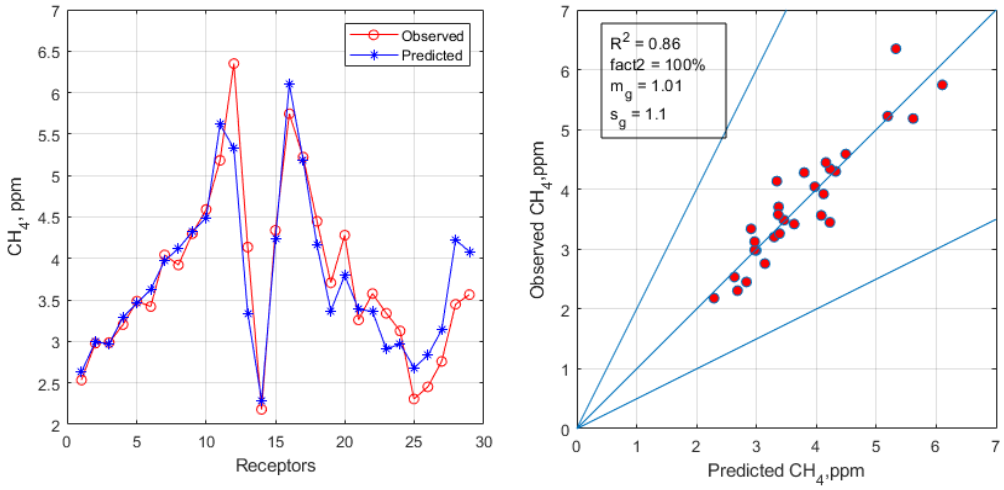

(a) **(b)**

Figure 2-3 (a) Performance of the EN model in describing the spatial distribution of measurements. (b) Scatter plot of modelled CH_4 and measured CH_4. The lines around the one-to-one line enclose model estimates within a factor of two of the measurements.

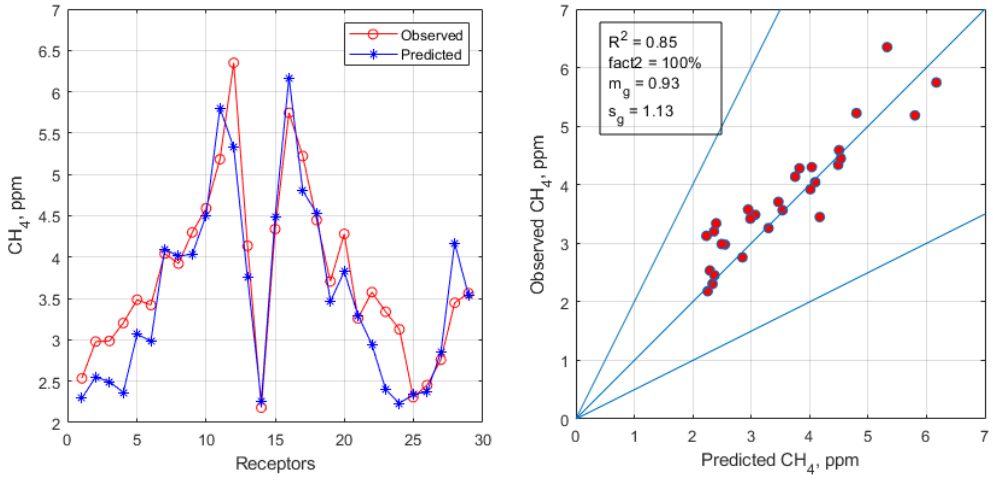

(a) **(b)**

Figure 2-4 (a) Performance of the bLS model in describing the spatial distribution of measurements. (b) Scatterplot of modelled CH_4 and observed CH_4. The lines around the one-to-one line enclose model estimates within a factor of two of the measurements.

Table 2-2 Inferred Emission Rates and Background Methane Mixing Ratio in Southern California Dairy. The 95% confidence limits of emission rates are normalized by the best fit value.

	Emissions				Uncertainty					
	EN Model		bLS Model		EN Model			bLS Model		
	kg/d	kg/m^2/yr	kg/d	kg/m^2/yr	Lower Limit	Upper Limit	Contribution to total emissions (%)	Lower Limit	Upper Limit	Contribution to total emissions (%)
Source 1	43	7.6	0	1.8	11.09	1.74	10.69	0.42	1.57	0.39
Source 2	55	9.7	1	1.4	14.19	1.42	14.14	0.59	1.39	19.85
Source 3	89	15.9	1	1.3	23.03	1.31	23.46	0.64	1.43	20.21
Source 4	200	36.0	1	1.2	51.81	1.18	51.56	0.84	1.17	59.58
Mean sum	**386**		**211**		0.73	1.25		0.82	1.17	
Back Ground (ppm)	**2.3**		**2.2**		0.83	1.20		0.83	1.19	

2.5.2 Central California Dairy

The dairy in central California consists of four manure lagoons shown in Figure 2-5(a). The manure wastewater flows from the bottom-most lagoon to the top and then to the left. Stationary measurements of atmospheric methane were made around these lagoons with the mobile laboratory at a total of 33 locations spread between 25th March 2019 and 30th March 2019. The averaging times for the stationary methane measurements were close to 10 minutes except at a few receptors. The bottom two lagoons were the most active and thus were divided into four parts for the modeling. Lagoon 1 comprises of Sources 1-4, Sources 5-8 form lagoon 2, Lagoon 3 is Source 9, and lagoon 4 is Source 10 as shown in Figure 2-5(b). Figure 2-5(b) shows the sources, receptor locations, anemometer location and the mean winds during the measurements. Table 2-3 shows the details of the sampling times, concentrations and the associated meteorological parameters.


Google Earth
N
200 m

(a)

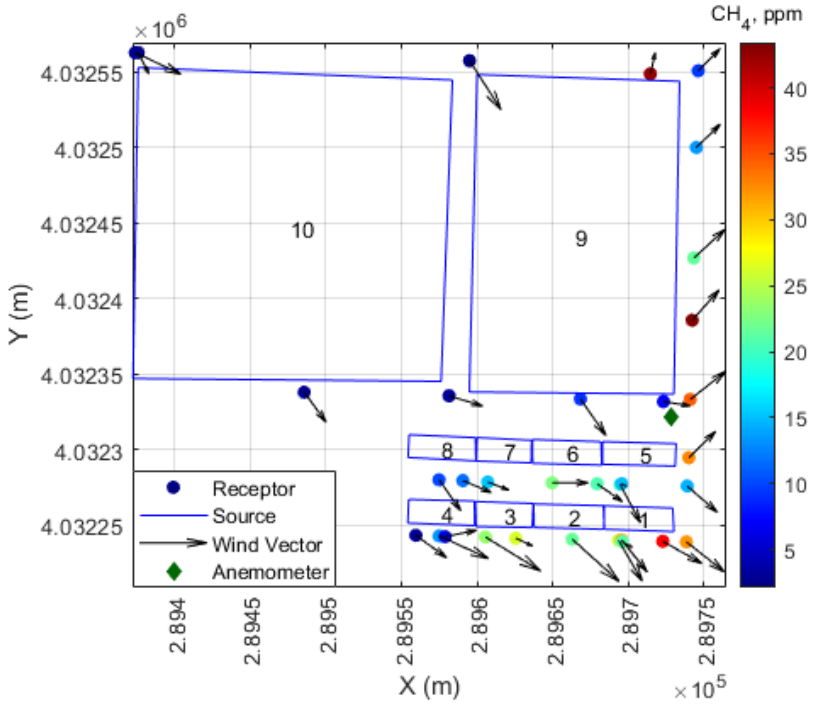
×10^6
4.03255
4.0325
4.03245
4.0324
4.03235
4.0323
4.03225
Y (m)
10
9
8
7
6
5
4
3
2
1
Receptor
Source
Wind Vector
Anemometer
2.894
2.8945
2.895
2.8955
2.896
2.8965
2.897
2.8975
X (m)
×10^5
CH4, ppm
40
35
30
25
20
15
10
5

(b)

Figure 2-5 (a) Aerial view of the manure lagoons in the Central California dairy. Red arrows show the flow of manure. (b) Model setup showing the source, the receptors as circles color coded by concentration and the mean wind direction at each receptor denoted by black arrows.

Figure 2-6(b) and Figure 2-7(b) indicate that the EN model explains 90% of the measured variance while the bLS model explains 95%. 94% of the values predicted by the models are within a factor of 2 of the observed values. Overestimates by more than a factor of 2 occur at low observed methane concentrations which are at the upwind side of the lagoons. The geometric standard deviations of 1.39 and 1.35 for the EN and bLS model respectively indicate higher scatter in the predicted concentrations when compared to that at the Southern California Dairy. This is also reflected in the differences in the estimates and ranks of methane emissions from each of the nine sources from the two models. This might be related to the lower, variable winds measured at this site compared to those at the southern California dairy.

Table 2-4 shows that the total emissions from the EN model is 3903 kg/d which is close to the 3637 kg/d estimated by the bLS model. The estimates of methane emissions from each of the ten sources differ in the two models, although the ranking of their contributions to the total emissions is the same:. lagoon 1 (sources 1-4) has the highest total emissions; lagoon 2 (sources 5-8) the next highest, followed by lagoons 9 and 10. This ordering of total emissions is consistent with the flow of the manure in the treatment process (Figure 2-5(a)).

The background concentrations here refer to the methane concentrations in the air coming into the lagoon complex area, and the elevated background concentrations predicted by the model here clearly reflect contributions of methane emissions from several nearby dairies on the upwind sides of the facility. The EN model predicted a background range of 2.1 to

6.8 ppm, whereas the bLS model predicted a background range of 2.6 to 6.5 ppm. The background concentrations measured from the upwind receptor locations varied from 2.1 ppm to 5.6 ppm as the wind direction brought in emissions from different upwind dairies.

Table 2-3 Details of sampling times, concentrations and associated meteorological parameters at Central California Dairy

Receptor #	Start Time (hrs)	End Time (hrs)	Concentration (ppm)	Wind Speed (m/s)	σ_w (m/s)	Wind Direction (Degrees)	u_* (m/s)	MO Length (m)
03/25/2019								
1	12:33	12:44	2.92	1.6	0.21	306	0.17	-5.5
2	12:45	12:55	13.34	2.3	0.22	295	0.15	-4.0
3	12:56	13:06	23.54	2.8	0.21	302	0.18	-7.5
4	13:17	13:27	21.69	2.7	0.22	312	0.14	-4.3
5	13:28	13:38	25.55	2.0	0.21	330	0.14	-5.6
6	13:39	13:49	38.20	1.9	0.23	300	0.18	-7.2
7	13:50	14:00	32.15	2.1	0.21	308	0.15	-4.7
8	14:20	14:31	14.39	1.7	0.19	311	0.10	-1.9
9	14:32	14:42	20.27	1.9	0.18	332	0.10	-2.4
10	14:42	14:53	20.55	1.3	0.21	305	0.03	-0.1
11	14:53	15:04	22.73	1.6	0.19	270	0.16	-7.7
12	15:15	15:25	11.69	1.3	0.19	293	0.11	-1.8
13	15:26	15:37	10.05	1.6	0.19	325	0.10	-2.6
14	15:39	15:44	31.42	1.8	0.20	321	0.15	-8.6
15	17:52	18:03	32.73	1.6	0.15	226	0.14	-25.3
16	18:04	18:14	34.48	2.0	0.15	232	0.10	-33.1
17	18:14	18:24	43.41	1.7	0.14	222	0.13	53.6

18	18:25	18:35	21.51	1.8	0.15	227	0.11	31.0
19	18:36	18:46	13.32	1.4	0.10	226	0.06	7.0
20	18:46	18:57	9.45	1.3	0.08	225	0.05	5.6
21	19:00	19:23	42.48	0.9	0.08	193	0.05	4.1
03/30/2019								
22	13:46	13:56	9.24	1.9	0.21	325	0.12	-2.1
23	14:02	14:12	2.66	1.0	0.26	333	0.12	-1.7
24	14:14	14:24	2.70	1.6	0.22	324	0.07	-0.3
25	14:25	14:36	3.00	1.5	0.21	287	0.13	-2.1
26	14:37	14:48	6.69	1.2	0.24	279	0.11	-1.2
27	14:49	14:59	14.98	0.2	0.24	298	0.13	-1.7
28	15:00	15:11	15.12	1.0	0.23	291	0.22	-9.0
29	15:12	15:22	5.57	1.4	0.26	259	0.19	-5.9
30	15:23	15:33	26.27	0.8	0.22	294	0.14	-2.9
31	15:34	15:44	21.14	0.5	0.25	300	0.12	-3.3
32	16:21	16:31	2.61	2.2	0.21	295	0.15	-4.3
33	16:33	16:43	2.12	2.5	0.20	327	0.16	-9.6

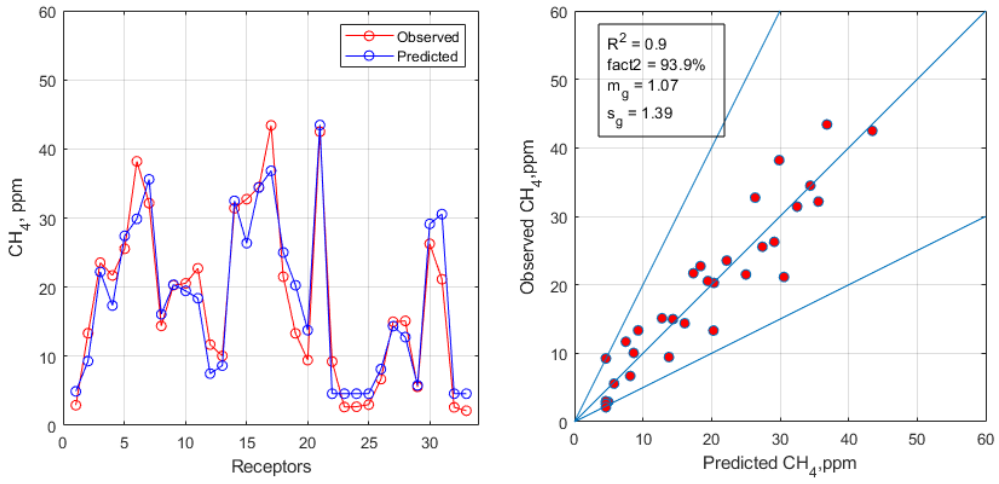

(a) **(b)**

Figure 2-6 Results from the EN model applied at the Central California Dairy: (a) Comparison of measurements and model results along the sampling points along the path of the mobile platform. (b) Scatterplot of model estimates and methane measurements. The lines around the one-to-one line enclose model estimates within a factor of two of the measurements.

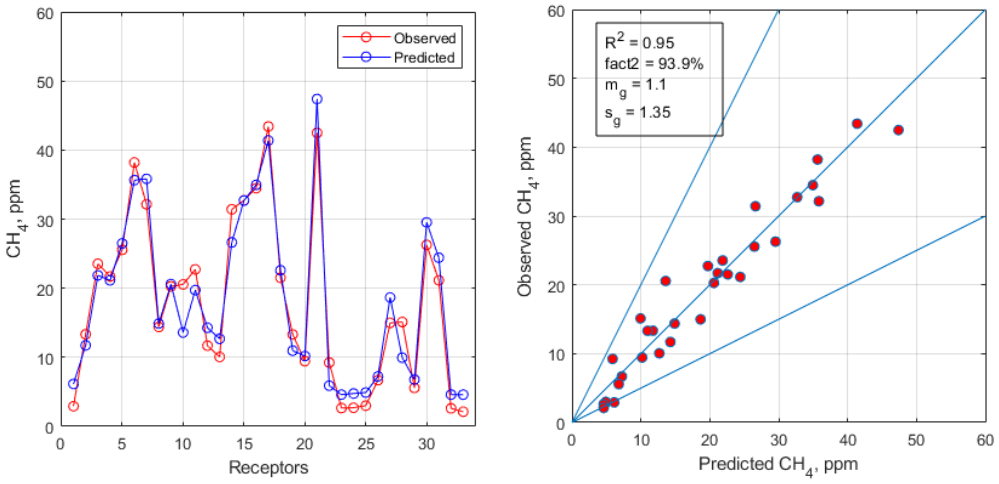

(a) **(b)**

Figure 2-7 Results from the bLS model applied at the Central Valley Dairy: (a) Comparison of measurements and model results along the sampling points along the path of the mobile platform. (b) Scatterplot of model estimates and methane measurements. The lines around the one-to-one line enclose model estimates within a factor of two of the measurements

Table 2-4 Inferred Emission Rates and Background Methane Concentration in Central California Dairy from the EN and bLS Models. The 95% confidence limits of emission rates are normalized by the best fit value.

	Emissions				Uncertainty					
	EN Model		bLS Model		EN Model			bLS Model		
	kg/d	kg/m^2/yr	kg/d	kg/m^2/yr	Lower Limit	Upper Limit	Contribution to total emissions (%)	Lower Limit	Upper Limit	Contribution to total emissions (%)
Source 1	751	384.2	858	440.5	0.73	1.24	19.25	0.85	1.14	23.60
Source 2	179	90.2	0.00	0.00	0.00	2.42	4.58	-	-	0.00
Source 3	596	355.0	635	404.1	0.54	1.41	15.26	0.75	1.26	17.45
Source 4	551	287.8	519	269.0	0.55	1.43	14.12	0.71	1.38	14.27
Source 5	313	157.8	130	64.7	0.35	1.70	8.01	0.24	1.89	3.58
Source 6	806	413.3	565	289.4	0.62	1.37	20.64	0.79	1.16	15.53
Source 7	211	139.1	69	45.3	0.00	3.15	5.40	0.00	3.63	1.90
Source 8	196	105.5	274	151.3	0.00	2.19	5.02	0.42	1.64	7.54
Source 9	0.00	0.00	283	3.7	-	-	0.00	0.05	1.76	7.77
Source 10	0.00	0.00	0.00	0.00	-	-	0.00	-	-	0.00
Mean sum	**3903**		**3637**		0.82	1.36		0.81	1.37	

Back Ground (ppm)	**4.58**		**4.60**		0.45	1.48		0.57	1.41	

2.6 Discussion

We used two state-of-the-art dispersion models, an Eulerian Numerical (EN) model and a backward Lagrangian Stochastic (bLS) model to infer methane emissions from manure lagoons located in dairies in Southern and Central California. The emissions are obtained by fitting model estimates to corresponding methane concentrations measured at several receptors surrounding the lagoons. The 95% confidence intervals for these emission estimates were computed by bootstrapping the residuals between model estimates and measurements.

The total emission rates of methane from the manure lagoons inferred by the two model differ by a factor of almost 2 in the Southern California Dairy although both models explain more than 85% of the variance of the measured methane concentrations. The inferred total emissions from the manure lagoons are close to each other in the Central California Dairy, although there are differences in the emission estimates from the source regions within the lagoons.

Other authors have compared emission rates from area sources using different models. Faulkner et al., (2007) compared ammonia emission fluxes (emission rate per unit area) from a feedlot inferred from four dispersion models using ammonia concentrations measured downwind of the feedlot over a 24 hour period in August 2002. They found that, as expected, the emission estimates depended on the model. AERMOD (Cimorelli et al. 2005), which uses semi-empirical vertical plume spreads based on the Project Prairie Grass (PPG) data (Venkatram 1992), yielded an emission rate that was 20% larger than that from

WindTrax. Bonifacio et al., (2013) conducted a one-year study to compare PM_{10} emission fluxes from a feedlot and found that AERMOD derived fluxes were about 30% higher than those from WindTrax for all stabilities; the fluxes were also highly correlated with an $r^2 > 0.88$. The results from these two studies are relevant to those presented in this paper because the vertical plume spreads in AERMOD are derived by fitting asymptotic solutions of the diffusion equation to the Prairie Grass data. They suggest that emission estimates from the diffusion equation are generally higher than those from the backward particle model in WindTrax. This trend is evident in the results from the Southern California dairy but is not clear in those from the Central California dairy.

The differences in the results from the two approaches, diffusion equation and Lagrangian particle model, are discussed by Sawford (2001) and Mooney and Wilson, (1993). The bLS model mimics turbulent dispersion by tracing the path of particles in turbulent flow using a stochastic differential equation. The EN model, on the other hand, is based on the concept of eddy diffusivity, which can be justified only when the travel time from the source is much larger the relevant Lagrangian time scale; its success in describing dispersion from surface releases (Nieuwstadt and Ulden 1978) provides posteriori justification. Thus, in principle, the bLS model is based on a more rigorous approach than the EN model. Sawford (2001) shows that the results from the diffusion model differ from the particle model even for surface releases: estimates of concentrations near the surface from the diffusion model are about 25% smaller than those from the particle model at the distances considered in the Project Prairie Grass (PPG) field study (Barad, 1958) when the surface layer is unstable. However, he found that in order to reproduce the vertical profiles measured in the PPG

study, it was necessary to increase the diffusivity, used to compute the Lagrangian time scale, by an empirical factor. Thus, for the time being, comparison of model results with concentration measurements has not established the superiority of the particle model for the application considered in this paper; the diffusion equation provides an excellent description of measured concentrations associated with surface releases.

The 95% confidence intervals computed for the emission estimates from each of the models are derived by bootstrapping the residuals between model estimates and corresponding measurements. Thus, they correspond to a combination of factors that affect the residuals: uncertainties in model formulation, model inputs, concentration measurements, locations and frequency of sampling, and temporal and spatial variation of the emissions from the lagoons. Identifying the major source of uncertainty would be speculation at this point.

We compared our results with lagoon calculations according to a bottom-up estimate based on the number of cows and management practices of the dairy. In this inventory, annual CH_4 emissions from lagoons are a function of the population, which we multiply by the fraction of manure entering the lagoons, according to the following calculation:

$$CH_4(EmissionRate) = f_{lagoon}.p_{cows}.VSP.C_f.P_{CH_4}.\rho_{CH_4} \quad (2.9)$$

where f_{lagoon} is the fraction of manure that ends up in the lagoon, and p_{cow} is the population of dairy cows. The other variables in the equation are VSP, which is the volatile solids production rate assigned its default value of 2833 kg/ year, C_f, the methane conversion factor taken to be 0.748, and P_{CH_4}, the maximum methane production capacity taken to be 0.24 m^3/kg, and the density of methane, ρ_{CH_4} taken to be 662 g/m^3.

The southern California dairy, with 1066 milking cows, is an open lot dairy, where most of the manure is dropped on the field. Manure from the milking parlor and the feedlots are flushed in the lagoon. We estimate $f_{lagoon} = 0.33$, which yields a methane emission rate of 324 kg/d, which lies between the best fit values of 211 kg/d and 386 kg/d from the two dispersion models.

The Central Valley dairy has 3200 milking cows that have access to both corrals and a free stall barn. In temperate and dry weather, the cows spend up to 42% of their time outside, where their manure remains in the corrals. However, during the winter months, the cows are only allowed in the free stall barns, which suggests that 100% of the manure is stored in the lagoons. Because March is the beginning of the spring season, much of the winter manure will still be in the lagoons. Assuming that f_{lagoon} lies between 0.58 and 1 yields methane estimates between 1712 kg/d and 2952 kg/d. The model best fit estimates are 3637 kg/d and 3903 kg /d.

3 Impacts of Noise Barriers on Near-road Air Quality

3.1 Introduction

Air pollution from roadways is a major source of pollution in urban areas. Exhaust emissions from vehicles on roads contain ozone precursors, NO_X and volatile organic compounds, as well as directly emitted particulate matter. The elevated levels of air pollutants near the freeway have been linked to a variety of adverse health effects (Chen et al., 2019; Brandt et al., 2014). Because a quarter of households in the metropolitan United States living within 300 feet of a 4- or more lane roadway (Bucholtz et al. 2011), it is important to examine methods that can mitigate the impact of vehicle emissions on near-road air quality.

Near road noise barriers have become common in California. Although these barriers are primarily designed to reduce noise from traffic on freeways, recent studies indicate that they a mitigating impact on the near-road vehicular pollution (Baldauf et al. 2008; Heist et al. 2009; Finn et al. 2010; Hagler et al. 2011).

Transportation conformity refers to the requirement under the Clean Air Act that federally supported highway and transit projects are consistent with the state air quality implementation plan (USEPA 2015). Because modeling the impact of emissions resulting from such projects is the US EPA suggested approach for transportation conformity it is

important to account for the effects of near-road barriers in this modeling exercise. A non-regulatory version of AERMOD (Cimorelli et al. 2005), the US EPA's regulatory model for short range dispersion, includes semi-empirical formulations to account for the effects of the noise barrier. This version of the model is based on data from wind tunnel and tracer experiments. Before it can be used for regulatory applications, it has to be evaluated and improved, if necessary, with data collected in a field study that includes features of the real world such as the complex geometry of the urban highway and unsteady meteorological conditions. This chapter summarizes my contribution to conducting such a field study and the subsequent analysis of the data from the field study.

3.2 Background and Approach

Results from a tracer study in which the noise barrier was simulated with a 6 m hay bale barrier indicate that near-road noise barriers have a mitigating impact on near road concentrations (Finn et al. 2010): the concentrations relative to those in the absence of the barrier were reduced by as much as 80% next to the barrier and about an average of 70% over a downwind distance of 30 times the barrier height. A wind tunnel study examining the effects of different road configurations observed concentration reductions ranging from 40% next to the barrier to 20% at downwind distances of 40 times the barrier height (Heist et al. 2009). A field experiment on adjacent sections of highways with and without noise barriers showed lower concentrations downwind of the noise barrier (Baldauf et al. 2008).

The wind tunnel study (Heist et al., 2009) showed that noise barriers reduce ground-level concentrations downwind of the barrier by lifting the plume from a line source over the

barrier. This plume is then entrained into the recirculating wake of the barrier resulting in a concentration profile that is relatively uniform through the height of the barrier. This well mixed region persists for downwind distances of about ten times the barrier height. The qualitative features of these observations have been have been reproduced by Hagler et al., (2011) using a Computational Fluid Dynamics (CFD) model. Laboratory simulation of plume using water channels also indicated that barriers created significant recirculating flow and updrafts resulting in enhanced turbulence and mixing (Pournazeri and Princevac 2015) that results in the reduction of ground-level concentration.

The data from the tracer field study (Finn et al. 2010) and the wind tunnel (Heist et al. 2009) form the basis of a semi-empirical model that accounts for the effects of a barrier on dispersion of emissions from a highway (Schulte et al. 2014). This model overpredicted concentrations during unstable conditions near the barrier. Amini et al., (2016) improved this model, reducing the over predictions near the barrier during unstable conditions, and evaluated the model by conducting a field experiment measuring ultrafine particles (UFP) from vehicles, downwind of a real-world barrier next to a freeway. Because of the uncertainty involved in estimating the UFP emission factor of vehicles, it was inferred by fitting model results to corresponding UFP concentrations.

The major features of the model developed by Schulte et al., (2014) have been incorporated into a non-regulatory version of AERMOD (Cimorelli et al. 2005), the USEPA's regulatory model for short range dispersion. The performance of this version of the model has not yet been evaluated under real-world conditions in which the geometry of the urban highway as well as the meteorological conditions are far from the idealized conditions of the tracer

field study and the wind tunnel. This chapter describes a tracer field study designed to collect the data required to evaluate the performance of AERMOD under these conditions. We have also conducted a preliminary evaluation of the resulting data set using a dispersion model that accounts for the effects of a barrier.

The next section describes the formulation of a semi-empirical model that accounts for the effects of the barrier on the dispersion of vehicular emissions. The following section describes the tracer study that collected the required data next to a noise barrier running along the University of California, Riverside. The final section describes the evaluation of the barrier model with the data collected from the field study.

3.3 Scaled Barrier Model

This section describes the formulation of a dispersion model that accounted for the two major effects of the barrier: lifting of the plume above the barrier followed by the entrainment of material in the plume into the wake downwind of the barrier. First, we assume that the wind direction is perpendicular to an infinitely long barrier, which allows us to formulate the model in a two-dimensional framework. The plume undergoes a series of idealized processes as it is transported from the source to the receptor. It first disperses vertically without being affected by the presence of the barrier. At the barrier, the vertical concentration profile resulting from dispersion upwind of the barrier is lifted to the top of the barrier by simply changing the vertical coordinate system used in describing the release so that the origin is at the top of the barrier: the new coordinate $z' = z - h_o$, where h_o is the barrier height. The entrainment into the wake is modeled by scaling the concentration

profile above the barrier by a factor $f_q < 1$ to account for the mass flux below the barrier. The vertical distribution beyond the barrier is given by

$$\begin{aligned} F_z(x_d, z) &= f_q D_z(x_d, z'); \quad z > h_o \\ F_z(x_d, z) &= f_e f_q D_z(x_d, 0); \quad z \le h_o \\ D_z &= \frac{1}{\sqrt{2\pi} U_e \sigma_z} \left\{ \exp\left(\frac{-(z - z_s)^2}{2\sigma_z^2} \right) + \exp\left(\frac{-(z + z_s)^2}{2\sigma_z^2} \right) \right\} \end{aligned} \tag{3.1}$$

where x_d is the effective distance downwind of the barrier, σ_z is the vertical plume spread at this distance, U_e is the effective horizontal velocity above barrier height and f_e is the entrainment factor. The calculation of these parameters is described later.

Note that the concentration below barrier height is constant. If the entrainment factor $f_e = 1$, the concentration is continuous across $z = h_o$. A value of $f_e < 1$ results in a discontinuity in the concentration at the top of the barrier; this mimics the sharp increase in concentration at the top of the barrier observed in wind tunnel simulations (Heist et al. 2009). The scaling factor, f_q, can be derived by multiplying the expressions in Equation (3.1) by the effective velocities U_e and U_b above and below the barrier respectively, and then integrating them from 0 to ∞ to obtain a a mass balance based on unit emission rate from the source. Simplifying the mass balance results in

$$f_q + f_q f_e D_z(x_d, 0) U_b h_o = 1 \tag{3.2}$$

where the first term on the left-hand side corresponds to the horizontal mass flux above the barrier, and the second term is the flux below the barrier. The uniform velocity below barrier height, U_b, is taken to be the average velocity below the barrier height. The velocity

profile is based on Monin-Obukhov similarity theory, where the values of the roughness length, z_o, the friction velocity, u_*, and the Monin-Obukhov length, L, are based on upwind micrometeorological measurements modified to account for barrier effects as discussed later.

Equation (3.2) yields

$$f_q(x_d) = \frac{1}{1 + f_e D_z(x_d, 0) U_b h_o} \tag{3.3}$$

The formulation for f_e is discussed in the next section.

The concentration profile with and without the barrier are shown in Figure 3-1. The concentration below the barrier height is constant and is lower than the concentration without the barrier. Above the barrier height, the concentration distribution follows a Gaussian profile: $f_q D_z(x_d, z')$. Note that the concentration profile assumes its near ground release shape when the barrier height, h_o. Also, the effect of the barrier becomes small as $D_z(x_d, 0)$ becomes small at large downwind distances.

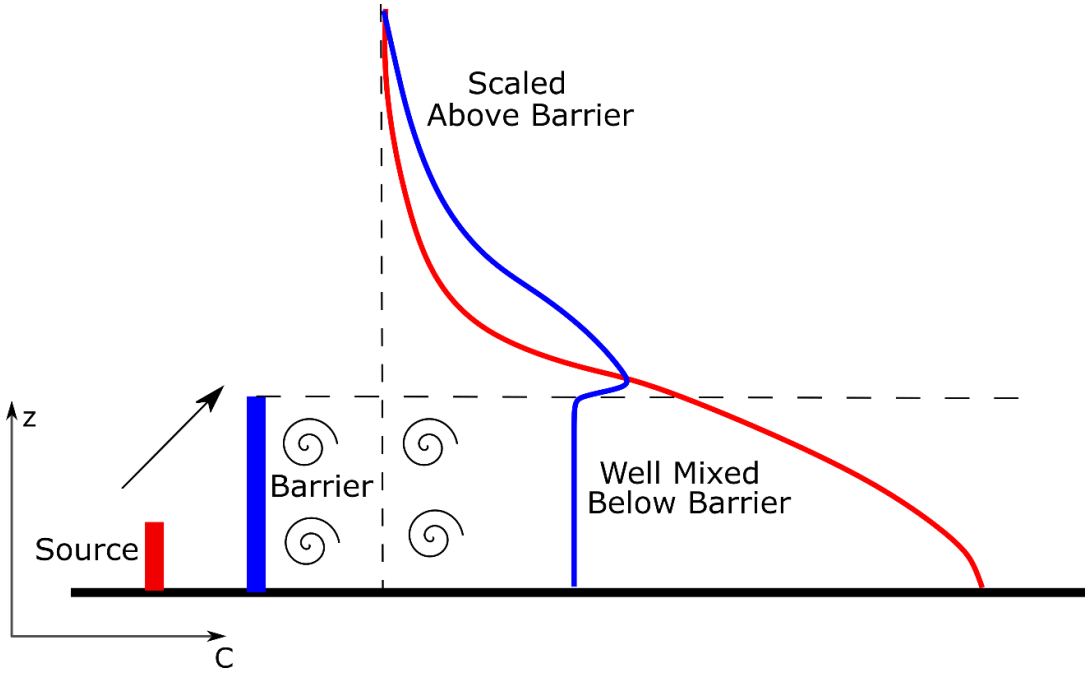

Figure 3-1 Schematic showing the vertical concentration distribution of the scaled barrier model. The swirls indicate the recirculation zone formed behind the barrier and the inclined arrow indicates the lifting of the plume up to the barrier height. The well-mixed layer below the barrier and scaled concentration above it are shown by the blue line while the red line represents the distribution without any barrier.

In the model, the highway is represented as a set of six-line sources. The contribution from each line source to the concentration at a receptor when the wind is not perpendicular to the line source is obtained from the approximate expression (Venkatram and Horst, 2006),

$$C(x,y,z) = \frac{q}{\cos(\theta)} \; erf\;\; t_1 \;\; - erf\;\; t_2 \;\;\; F_z \;\; x_d, z' \tag{3.4}$$

$$t_i = \frac{y_i - y}{\sqrt{2}\sigma_y \;\; x - x_i}$$

where q is the line source emission rate per unit length of the road, x and y are the receptor coordinates based on the coordinate system in which the x-axis is parallel to the wind

direction, 1 and 2 correspond to the endpoints of the line source, θ corresponds to the wind direction with respect to the x-axis, $y - y_i$ is the distance of the endpoints from the receptor along the direction perpendicular to the wind direction, $\sigma_y(x - x_i)$ is the horizontal plume spread (Venkatram et al. 2013b) at the distance of the receptor from the two endpoints along the direction parallel to the wind, and $F_z(x_d, z')$ is the vertical distribution function discussed earlier. The effective downwind distance from the barrier x_d, is the shortest distance along the wind direction between the receptor and the barrier.

The effective wind velocity, U_e in Equation (3.1) is given by,

$$U_e = \sqrt{2\sigma_v^{\,2} + U(\bar{z} + h_o)^2} \tag{3.5}$$

where $U(\bar{z})$ is the wind speed at the mean plume height, $\bar{z}$. The mean plume height, $\bar{z}$, is related to the vertical plume spread, which in turn is a function of U_e. So these parameters are computed iteratively (Venkatram et al. 2013b) from ,

$$\sigma_z = f\ \ x, u_*, L, U_e\ \ h_o$$

$$f(x, u_*, L, U_e) = \begin{cases} 0.57\dfrac{u_*}{U_e}\left(1 - 1.5\dfrac{u_*}{U_e}\dfrac{x}{L}\right); L < 0 \\ 0.57\dfrac{u_*}{U_e}x\left(1 + 3\dfrac{u_*}{U_e}\left(\dfrac{x}{L}\right)^{\frac{2}{3}}\right)^{-1}; L > 0 \end{cases} \tag{3.6}$$

$$\bar{z} = \sigma_z\sqrt{\frac{2}{\pi}}\exp\left(-\frac{1}{2}\left(\frac{z_s}{\sigma_z}\right)^2\right) + z_s erf\left(\frac{z_s}{\sqrt{2}\sigma_z}\right) \tag{3.7}$$

Equation (3.4) breaks down when $\theta = 90°$ because of the $cos\theta$ in the denominator. The term $\sigma_z cos\theta$ (Venkatram et al. 2013a) is modified as follows to avoid this,

$$\sigma_z(x_d)\cos\theta = \frac{\sigma_z(x_d\cos\theta) + \sigma_z(x_d)\cos\theta}{2} \tag{3.8}$$

Vertical mixing occurs when the plume travels from the line source to the barrier. This mixing is also enhanced by the movement of the vehicles on the freeway. To account for this an effective initial mixing distance, x_o is computed which is added to x_d. The vertical plume spread due to this vertical mixing is,

$$\sigma_{z_o} = \sqrt{f(x_s, u_*, L, U_e(0))^2 + h_v^{\,2}} \tag{3.9}$$

Where x_s is the downwind distance from the line source to the barrier and $h_v(= 1.5m)$ is the effective height of the vehicles traveling on the freeway. The value of x in Equation (3.10) that gives the σ_{z_o} computed in Equation (3.9) is x_o.

$$\sigma_{z_o} = f\ \ x, u_*, L, U_e\ \ h_o \tag{3.10}$$

3.3.1 u_* Correction

The presence of the barrier increases turbulent mixing downwind of the barrier as observed in various studies (Heist et al., 2009). This increase in turbulence is accounted for by increasing the friction velocity, u_* near the barrier as follows,

$$z_{ob} = \max\left(\frac{h_o}{9}, z_o\right) \tag{3.11}$$

$$u_{*_b} = u_* \left(\frac{z_{ob}}{z_o} \right)^{0.17} \tag{3.12}$$

The friction velocity was used to compute a modified Monin-Obukhov length assuming that the heat flux does not change. The modified friction velocity, u_{*b} recovers to its upwind value over a length scale determined empirically to be $5h_o$. Then,

$$u_{*_c} = u_{*_b} f_m + u_* \ 1 - f_m \tag{3.13}$$

$$f_m = \exp\left(-\frac{x_d}{5h_o} \right) \tag{3.14}$$

where u_{*c} is the corrected friction velocity used in computing vertical spread of the plume. The factor f_m tends to 1 near the barrier and zero at downwind distances that are several times the height of the barrier.

3.3.2 Entrainment Factor, f_e

When the wind speeds are low, we found that the model overestimated concentrations, which suggested decreasing the entrainment, i.e., $f_e < 1$. This effect is illustrated in Figure 3-2, which shows the ratio of the mean predicted concentration to the mean observed concentration (C_p/C_o) versus the friction velocity, u_*. The mean predicted concentration is close to 3.5 times the observed concentration when u_* is less than 0.1 m/s and these overpredictions reduce with increasing u_*. This suggested the following empirical relation,

$$f_e = \frac{u_{*_b}}{u_{*_b} + u_{*_o}} \tag{3.15}$$

where $u_{*o} = 0.1\ m/s$. f_e tends to 1 as u_* increases. Equation (3.15) is designed to reflect the possibility that the turbulence generated by wind shear at the top of the barrier becomes less effective in entraining the plume above the barrier as the wind speeds approach zero.

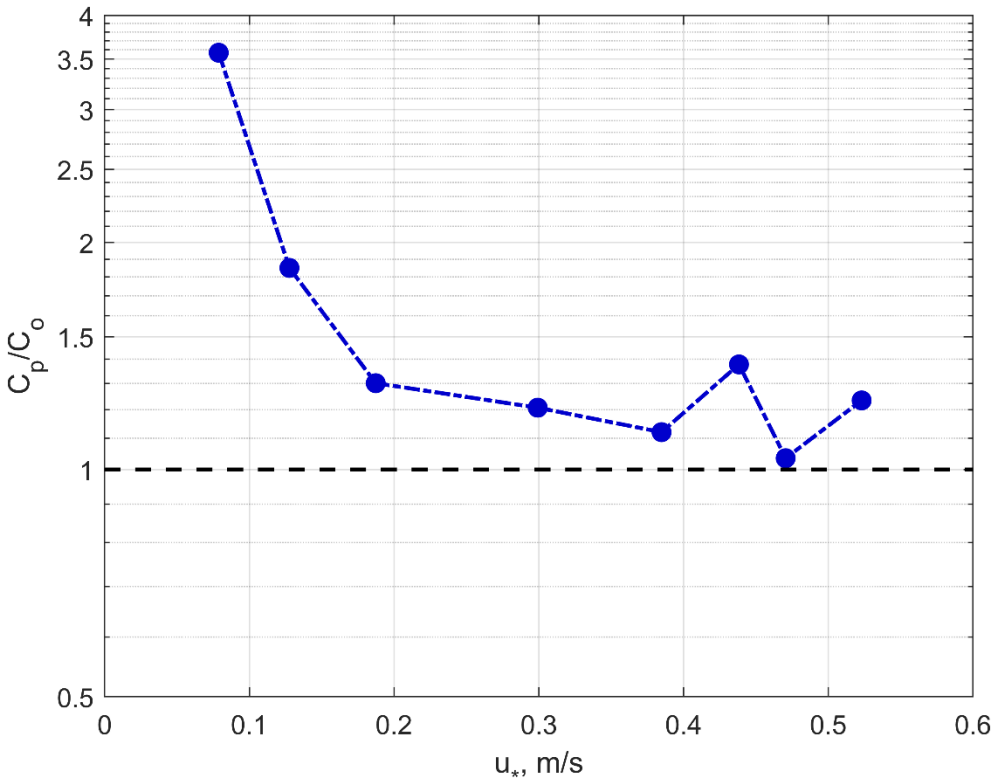

Figure 3-2 Plot between the ratio of the predicted to the observed concentration without the entrainment factor ($\boldsymbol{f_e = 1}$). The overpredictions decrease with increasing $\boldsymbol{u_*}$.

3.4 Field Study

This section describes a field study that was conducted next to a real-world barrier to collect the data necessary to evaluate the barrier model.

3.4.1 Site

The study was conducted on a portion of Interstate-215 freeway passing through the University of California, Riverside (UCR) campus. The freeway runs from north-northeast to south-southwest as shown in Figure 3-3. A single noise barrier almost parallel to the freeway is located towards the east of the freeway. The noise barrier is about 5 m high and is approximately 1.3 km long. The highway and the barrier curve to the west near the southern edge of the barrier. The three outermost lanes on each side of the freeway were used in the study. The aerial view of the study region is shown in Figure 3-3. The study was conducted on four different days to capture different atmospheric stability conditions. Table 3-1 provides the dates of the study days and the time intervals when the measurements were made.

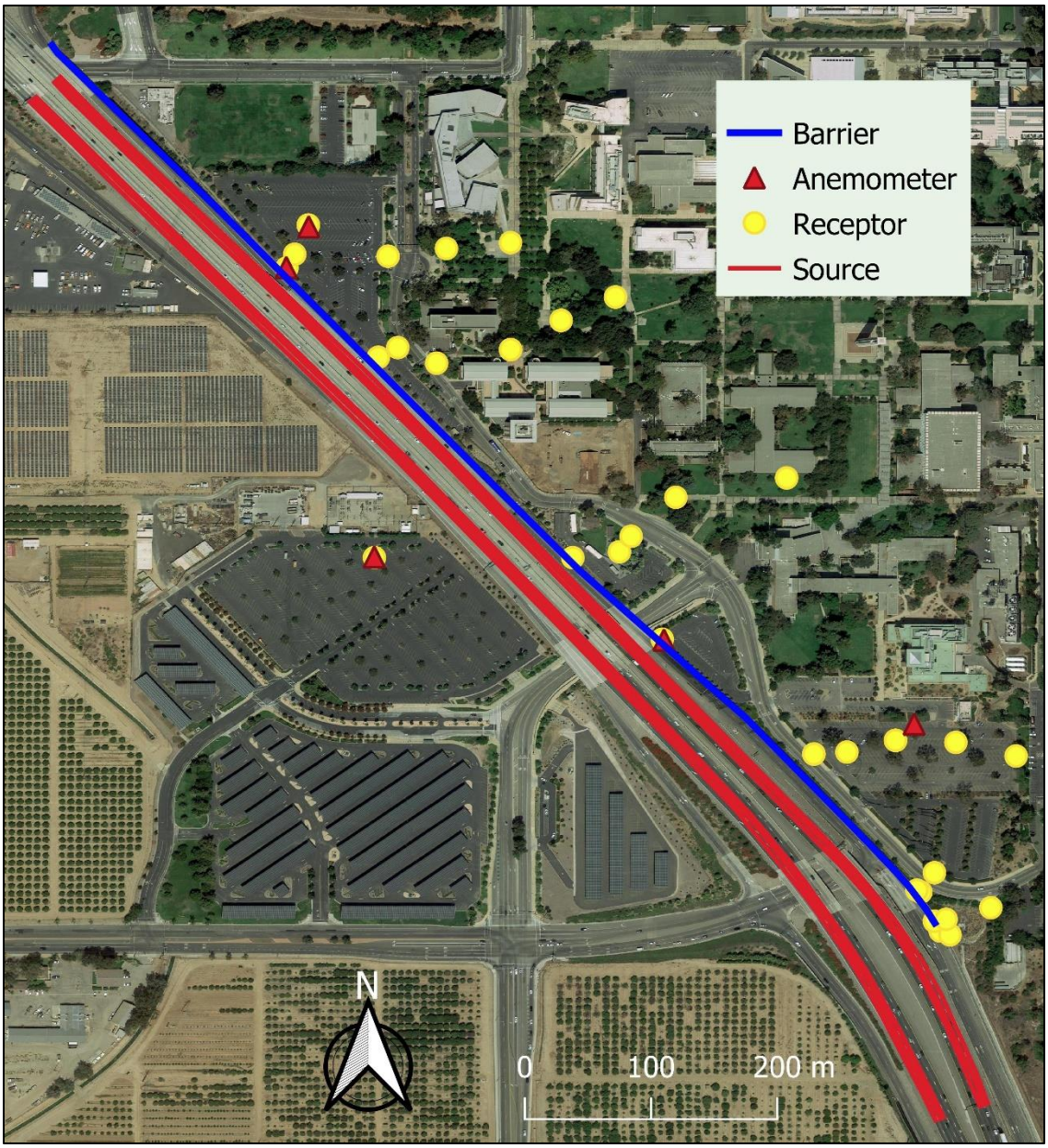

Figure 3-3 Aerial view of the study region. The receptor locations are shown using yellow circles, the red lines are the sources, the noise barrier is represented using a blue line, and the red triangles show the locations where the meteorological data was collected.

Table 3-1 Dates of study days and the measurement time intervals.

Date	**7/30/2019**	**8/6/2019**	**8/13/2019**	**8/20/2019**
Study Day	**1**	**2**	**3**	**4**
Exp 1 (Background)	13:00 - 13:30	15:00 - 15:30	20:00 - 20:30	18:00 - 18:30
Exp 2	14:00 - 14:30	16:00 - 16:30	21:00 -21:30	19:00 -19:30
Exp 3	14:30 - 15:00	16:30 - 17:00	21:30 - 22:00	19:30 - 20:00
Exp 4	15:00 - 15:30	17:00 - 17:30	22:00 - 22:30	20:00 - 20:30
Exp 5	15:30 - 16:00	17:30 - 18:00	22:30 - 23:00	20:30 - 21:00
Exp 6	16:00 - 16:30	18:00 - 18:30	23:00 -23:30	21:00 - 21:30

3.4.2 Tracer Release System

Custom-built tracer gas release systems were fitted to eight road vehicles. The release system consisted of a cylinder containing pure SF_6 with a pressure regulator as shown in Figure 3-4. The pressure regulator was attached to an electronic solenoid that could be controlled from inside the vehicle. The solenoid opened the gas flow to a mass flow controller that was controlled by an Arduino computer. A GPS unit on the roof of the vehicle fed the location data to the computer. The mass flow controller was programmed to provide a full release rate of 42 ml/s when vehicle speeds were above 100 km/hr. The release rate linearly reduced with decreasing vehicle speed to simulate exhaust emissions

from vehicles. The outlet flow from the mass flow controller was looped into the vehicle exhaust.

Eight vehicles fitted with the tracer release system were driven on the I-215 freeway. The vehicles started about 1-minute apart from each other to obtain a uniform release. The gas cylinders were weighed before and after each study period to determine the total gas release. The tracer gas released on each study day is shown in Table 3-2.

Table 3-2 Total tracer gas released on each study day

Day	Tracer Released (kg)
1	1.990
2	2.620
3	1.900
4	2.225

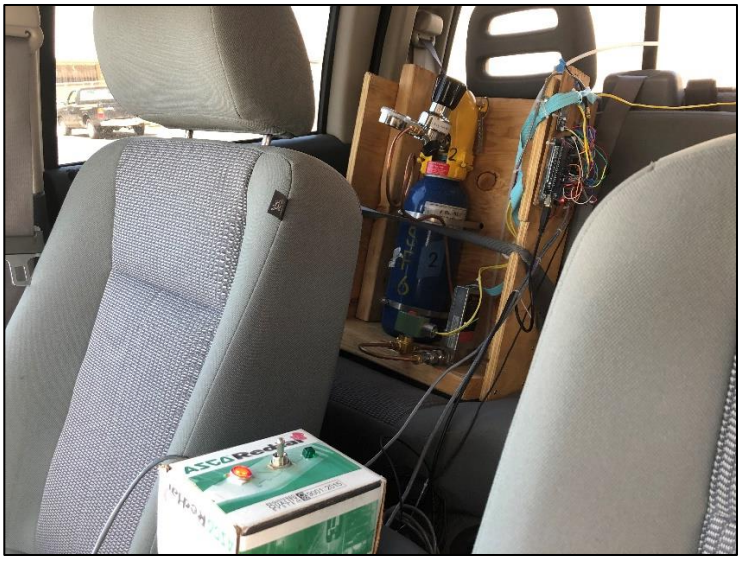

(a)

(b)

Figure 3-4 (a) Picture of the SF_6 gas cylinder with the pressure regulator, the electronic solenoid (green and white box) that could be operated from within the vehicle, and the mass flow controller. (b) The SF_6 gas from the mass flow controller was looped into the vehicle exhaust.

3.4.3 Samplers

A total of 46 air samplers were used in the study. The sampler locations on one of the study days is shown using in Figure 3-3. As winds were expected to be predominantly westerly, downwind samplers were placed east of the sound barrier while a single upwind sampler was placed west of the freeway. All the samplers had inlets at a height of 1.8m.

Each sampler consisted of 6 pumps and each pump was connected to a 12-liter polyethylene bag. An air sampler system used in the study is shown in Figure 3-5(a). A single-board computer (Z-World Rabbit Model 1810) with drivers to control each sample pump formed the timer system. The samplers were programmed to collect integrated 30-minute air samples. The first sample on each study day was collected 45 minutes before the start of the tracer release to measure the background while subsequent experiments were conducted every 30 minutes with the second experiment beginning 15 minutes after the start of the tracer release.

The collected samples were taken to a laboratory at UCR CE-CERT for analysis using the system shown in Figure 3-5(b). All six bags from three samplers could be sampled simultaneously using the custom-built auto-sampler system. Pumps and solenoid valves were used to control the flow of the samples. The samples were measured using a bank of Agilent Technology 6890N electron capture (ECD) gas chromatographs (GC) equipped with a 1/8-inch diameter Molecular Sieve 5A column and multi-port gas sampling valves to measure SF_6.

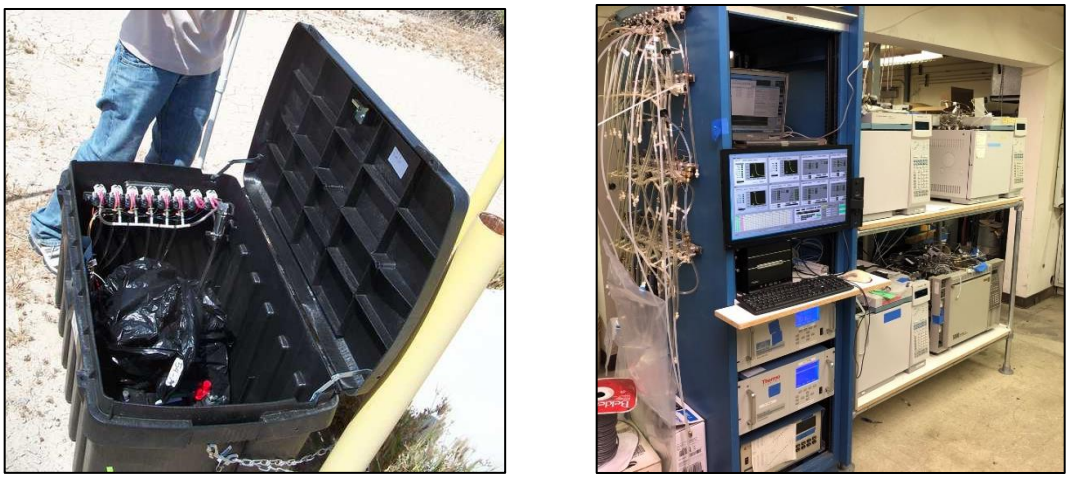

(a) **(b)**

Figure 3-5 (a) Inside of the sampler system containing six pumps and six bag samplers. (b) Custom built analysis system used in the study to measure SF_6 concentrations in the collected samples.

3.4.4 Meteorological and Air Quality Data

The meteorological data were collected using six 3-D Sonic Anemometers. The locations of the anemometers are shown in Figure 3-6. Two of the sonics (RM Young Model 81000) were placed towards the west (upwind) of the freeway mounted at 3 m and 5 m on a tower (Figure 3-6), while the four remaining sonics (Campbell Scientific Model CSAT3) were placed east (downwind) of the freeway at a height of 2 m. The meteorological data were recorded with a frequency of 20 Hz. The data from the upwind sonic at 5 m height were used in the dispersion model to interpret the data from the field study.

Figure 3-6 Upwind meteorological measurement site containing two 3-D sonic anemometers mounted at heights of 3 m and 5 m.

Table 3-3 summarizes the meteorological data collected by the upwind sonic at a height of 5 m where, Q_o is the kinematic heat flux, u_* is the friction velocity, and L is the Monin-Obukhov length. On Days 3 and 4, the measurements were conducted in the late evening hours when the sun had set, but the surface heat fluxes remained positive, athough they were relatively small. This suggests that heat fluxes in this urban area are affected by advection of colder rural air onto a warmer urban surface.

On Day 3, the wind speeds and consequently the surface friction velocities were relatively small compared to the values on the other days. This has an impact on model performance described below.

Table 3-3 Summary of meteorological data collected at the upwind side of the freeway at a height of 5 m.

Exp	Day 1			Day 2		
	Q (K.m/s)	u_* (m/s)	L (m)	Q (K.m/s)	u_* (m/s)	L (m)
1	0.260	0.30	-8.0	0.215	0.45	-34.2
2	0.261	0.45	-27.7	0.215	0.53	-56.0
3	0.263	0.52	-41.1	0.188	0.51	-56.7
4	0.257	0.49	-36.2	0.170	0.47	-48.5
5	0.218	0.47	-37.8	0.133	0.44	-49.6
6	0.227	0.46	-34.0	0.110	0.47	-73.1
Exp	**Day 3**			**Day 4**		
	Q (K.m/s)	u_* (m/s)	L (m)	Q (K.m/s)	u_* (m/s)	L (m)
1	0.039	0.18	-11.9	0.098	0.38	-43.1
2	0.019	0.14	-10.3	0.052	0.38	-84.1
3	0.008	0.11	-10.7	0.029	0.30	-70.6
4	0.016	0.13	-9.5	0.028	0.19	-17.9
5	0.005	0.10	-12.4	0.027	0.19	-19.0
6	0.011	0.06	-1.5	0.011	0.14	-21.0

Figure 3-7 shows the variation of the measured SF_6 concentration as a function of the distance from the barrier. The vertical axis represents the ratio of the measured concentration to the maximum concentration observed during a 1-hr averaging period and the horizontal axis represents the perpendicular distance from the barrier.

The solid line represents the same ratio using a dispersion model (Venkatram and Schulte 2018) that accounts for the effect of the barrier as follows,

$$C(x_b) = \sqrt{\frac{2}{\pi}} \frac{q}{W\sigma_w} \ln\left(1 + \frac{W}{x_b + \frac{h_o U_e \cos\theta}{\sigma_w}}\right) \tag{3.16}$$

where q is the emission rate per unit length, h_o is the barrier height, x_b is the perpendicular distance from the barrier, W is the width of the road, σ_w is the standard deviation of the vertical wind fluctuations, θ is the angle between the wind direction and the perpendicular to the road and U_e is the effective wind speed. The maximum concentration, used to normalize $C(x_b)$ is $C(0)$.

The model implies that the primary effect of the barrier is to shift the road sources upwind by a distance, $h_o U_e cos\theta/\sigma_w$. We see that the downwind variation of the concentrations is consistent with this idea. The next section describes a model that includes more of the governing processes.

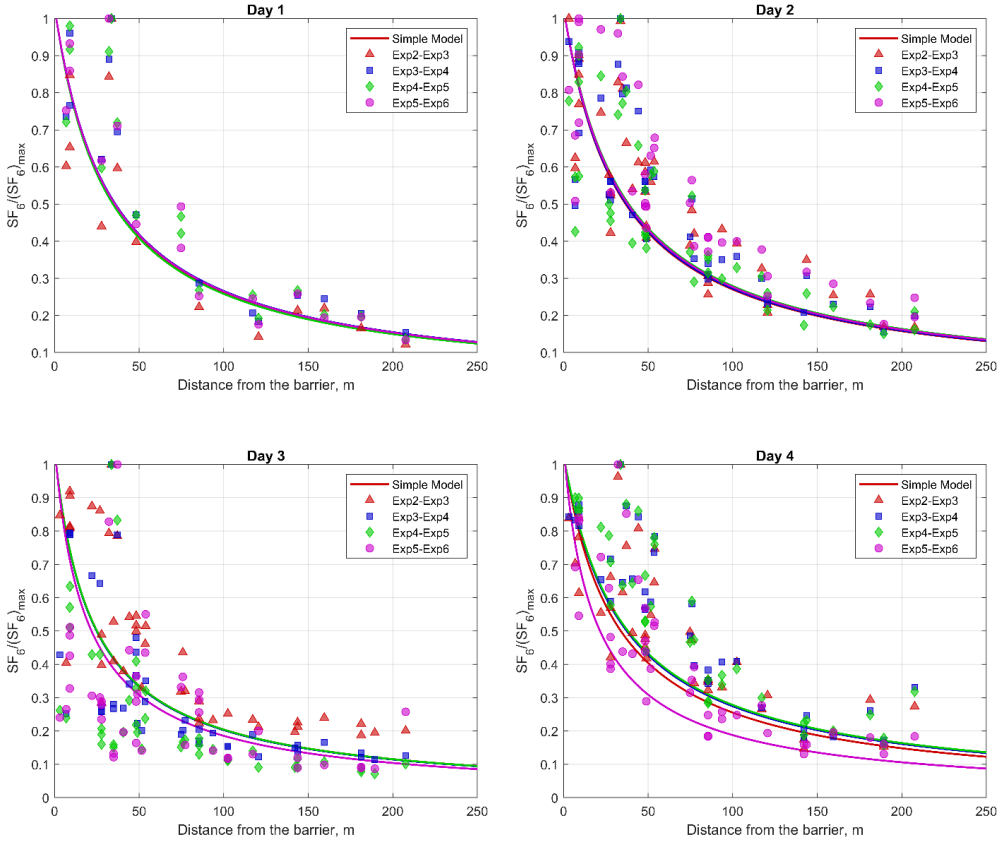

Figure 3-7 Plot between the ratio of measured concentration to the maximum concentration observed during the 1-hr averaging period, and the downwind distance from the barrier. The colored symbols represent the 1-hr averaged measured concentration while the solid lines represent the ratio from Equation 1. The color of the solid line represents the measurement period and uses the same color code as the measured values.

3.5 Model Performance and Barrier Effects

The performance of the barrier model formulated in Section 3.3 is summarized in Table 3-4 using the coefficient of regression between the one hour averaged observed and predicted SF_6 concentration, R^2, and median of the ratio between the one hour averaged predicted and observed SF_6 concentration, m_g. The deviation of m_g from 1 quantifies the overall bias in the model. An m_g value less than 1 points to underprediction and an m_g

value greater than 1 indicates overprediction. On Days 1 and 2, the model performs well both with and without the entrainment factor. The R^2 and m_g are 0.90 and 0.99 respectively on Day 1 without the entrainment factor, and are 0.91 and 0.88 with the entrainment factor. The R^2 and m_g are 0.75 and 1.12 on Day 2 without the entrainment factor, and 0.75 and 1 with the entrainment factor.

The model has large overpredictions on Day 3 without the entrainment factor with a m_g of 2.21 and a low R^2 of 0.49. When the entrainment factor is included in the model, performance improves with a m_g of 1.35 and an R^2 of 0.53. On Day 4, the inclusion of the entrainment factor improves the results with the R^2 and m_g changing from 0.87 and 1.19 without the entertainment factor to 0.89 and 0.93 with the entrainment factor.

Figure 3-8 shows the plot with the SF_6 concentration on the vertical axis and the distance from the barrier on the horizontal axis. The concentration data was averaged based on the distance from the barrier using 25 m long bins. The observed concentrations are represented by red circles while the predicted concentrations are represented by blue squares. The plots on the left panels show results without the entrainment factor, i.e., $f_e = 1$ and the plots on the right show results with f_e given by Equation (3.15). The overpredictions on day 3, when the wind speeds are low, are reduced when the entrainment factor is incorporated, as seen in the right panel.

Table 3-4 Performance statistics between 1-hr averaged observed concentration with the 1-hr averaged predicted concentration from the scaled barrier model.

	Without Entrainment Factor		**With Entrainment Factor**	
	R^2	m_g	R^2	m_g
Day 1	0.90	0.99	0.91	0.88
Day 2	0.75	1.12	0.75	1.00
Day 3	0.49	2.21	0.53	1.35
Day 4	0.87	1.19	0.89	0.93

The effect of the barrier was studied by running the barrier model with no barrier $(h_o = 0, Open)$ and comparing with results with the barrier $(h_o = 5, Barrier)$. The predicted concentration without the barrier is represented by green triangles in Figure 3-8. The reduction in concentration due to the barrier is more than 50% close to the freeway and becomes very small at downwind distances greater than 150 m. These results are consistent with previous studies on barriers (Baldauf et al. 2008; Heist et al. 2009; Finn et al. 2010).

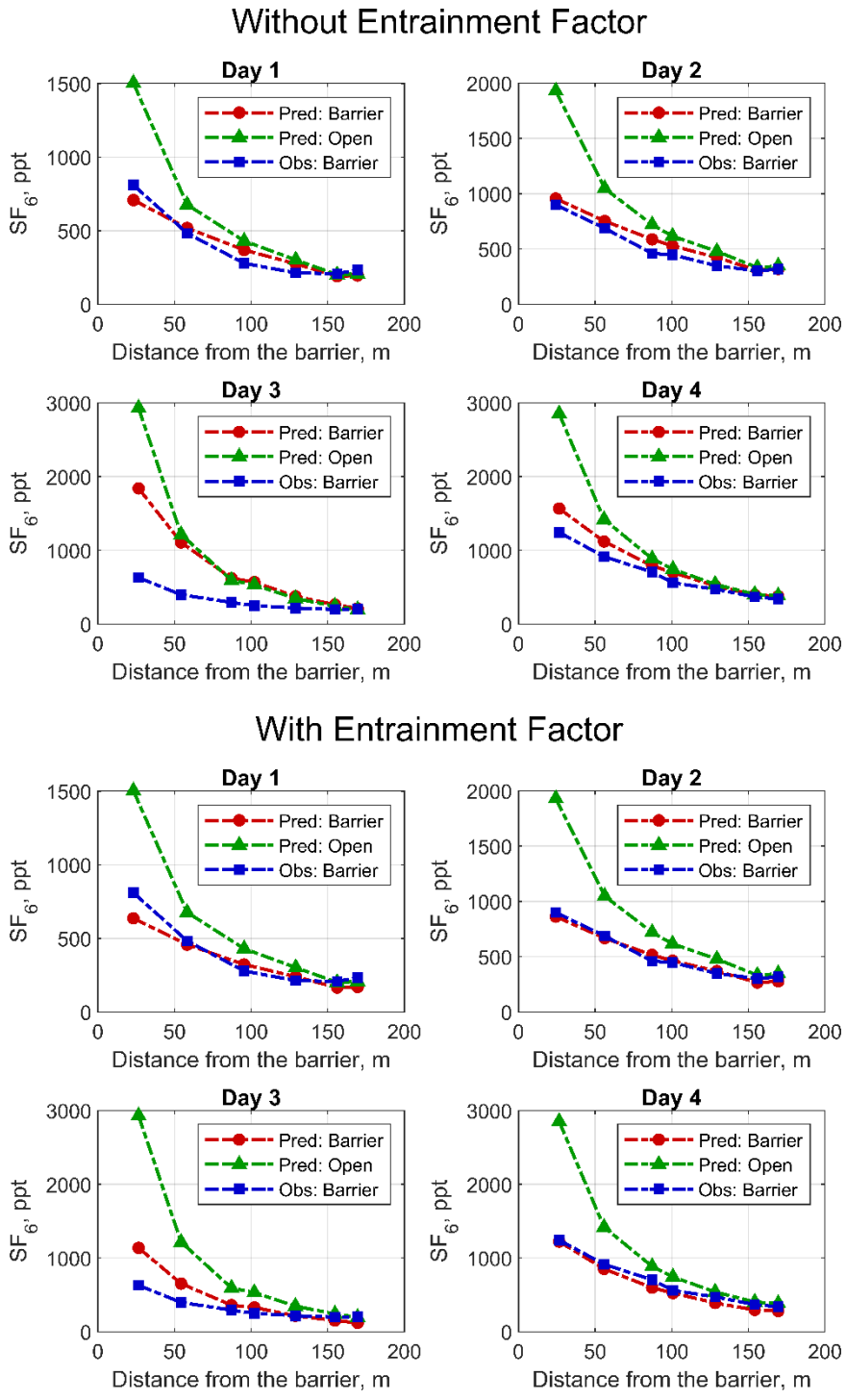

Figure 3-8 Plot showing the SF_6 concentration with the distance from the barrier. The observed concentration with the barrier is shown by blue squares, the predicted concentration with the barrier is shown by red circles, and the predicted concentration without the barrier is shown by green triangles.

3.6 Conclusions

In this chapter we formulated a plum based dispersion model to account for the effects of the solid nose barriers on the dispersion of vehicular emissions from roadways. We then performed a tracer study next to a real-world barrier to collect the data required to evaluate the barrier model. The barrier model was evaluated using the data collected in the tracer studies and was found to explain the observed concentration well. This study forms the first step towards including algorithms to incorporate the effects of solid noise barriers in regulatory models.

4 Estimating Micrometeorological Inputs for Dispersion Models

4.1 Introduction

Application of dispersion models requires meteorological inputs such as wind speed, friction velocity and heat flux (Cimorelli et al., 2005). In principle, these inputs can be inferred from multi-height measurements of wind speed and temperature. These inferences are based on Monin-Obukhov Similarity theory (MOST, Businger, 1973; Holtslag and van Ulden, 1985). MOST is based on the idea that measured gradients of mean horizontal wind speeds and temperatures become "similar" when they are expressed in terms of non-dimensional variables obtained by scaling them with appropriate velocity, temperature, and length scales. These scales are related to the fluxes of heat and momentum at the surface. Integrating the nondimensional gradients yields profiles of horizontal velocity and temperature. Thus, in principle, measurements of velocity and temperature at several heights can be used to infer surface heat and momentum fluxes, which in turn can be used to estimate the variables required in dispersion models.

Although MOST holds strictly over horizontally homogeneous surfaces over which these fluxes are relatively uniform, the theory has been applied to other conditions because it provides reasonable estimates of the surface fluxes. But the estimates of momentum and

heat fluxes from measured mean profiles are prone to errors when the differences between levels are small during convective conditions. The micrometeorological inputs can also be computed using measurements made with 3-D sonic anemometers. The reliability of these measurements depends on careful alignment of the anemometer arms to avoid the contamination of vertical velocity fluctuations, used to compute heat flux, by horizontal velocity fluctuations. Alignment of the 3-D sonic anemometer might not be possible especially when the ground is not firm or uneven. Thus, there is a need for a method that avoids these problems and is accurate enough for its intended application.

The uncertainty in meteorological inputs might not be critical in regulatory applications in which producing realistic concentration distributions is more important than describing concentrations paired in space and time. In some applications of dispersion models, such as the ones considered in this study, this uncertainty needs to be minimized by using on-site meteorological measurements.

The major motivation for the development of the micrometeorological model described in this work is the growing popularity of mobile monitoring platforms (MMF) in air quality studies. For example, Brantley et al., (2014) used mobile monitoring to survey oil and gas production facilities to estimate leaks of methane. U.S. EPA's Other Test Method (OTM33; 33 and 33A Geospatial Measurement of Air Pollution-Remote Emissions Quantification-Direct Assessment (GMAP-REQ-DA). 2014. (http://www.epa.gov/ttn/emc/prelim.html) for estimating fugitive emissions relies on mobile monitoring.

In the work we performed to characterize methane emissions from dairy manure lagoons, we describe the use of a mobile platform to estimate methane emissions from manure lagoons in dairies. In such studies (Amini et al., 2022), the unknown emissions are generally inferred from the concentration measurements using a dispersion model. The meteorological inputs for the dispersion models are estimated from a stationary 3-D sonic anemometer or from routine measurements made at the nearest airport. It is clearly better to have these meteorological inputs derived from instrumentation placed on the mobile monitor. The micrometeorological method that we describe in this paper is suited for mobile applications in which the set-up and dismantling of meteorological instrumentation is relatively simple, can be performed quickly, and is not prone to errors.

4.2 Background and Approach

Application of currently used dispersion models, such as AERMOD (Cimorelli et al. 2005) and ADMS (Carruthers et al. 2011) require meteorological inputs such as wind speed, friction velocity and heat flux. In the absence of on-site measurements from 3-D sonic anemometers, these inputs are constructed with AERMET (meteorological data preprocessor for AERMOD) using variables such wind speed, wind direction, and cloud cover, that are routinely measured at an airport close to the site where AERMOD is being applied. AERMET uses a one-dimensional boundary layer theory to convert these measurements into micro-meteorological inputs required by AERMOD. These inputs include the surface friction velocity, the sensible heat flux, the convective velocity scale, the Monin-Obukhov length, and the convective and mechanical boundary layer heights. The output from AERMET is likely to differ from that applicable to the site where

AERMOD is being applied for two major reasons: 1) the inputs to AERMET, such as mean wind speed and direction will differ from those at the nearest airport, especially if the airport is far away from the site, 2) the one-dimensional boundary layer model used in AERMET might not be applicable to the site. For example, the boundary layer model in AERMET does not account for shoreline effects that are important if AERMOD is applied to examine sources next to a water-land interface.

Recognition of the inadequacy of the one-dimensional boundary layer model of AERMET has prompted the development of methods to infer AERMOD inputs using the outputs of prognostic meteorological models (Isakov et al., 2007; Touma et al., 2007). These studies suggest that the outputs from one of the models studied, MM5, can be processed to provide AERMOD inputs that provide concentration estimates that compare favorably with those from onsite measurements; however, onsite meteorological measurements are preferable to outputs from a meteorological model.

In this study, we re-examine a technique that estimates heat and momentum fluxes with measurements of temperature fluctuations and horizontal wind speeds at a single level. Methods based on single level temperature and velocity measurements have been proposed by several authors ever since Monin and Yaglom (1971) proposed the relationship between heat flux and temperature fluctuations measured under unstable conditions. Tillman (1972) extended this relationship through a semi-empirical correction to account for finite friction velocities. Tillman (1972) and Albertson et al. (1995) showed that measurements of moments of temperature fluctuations can be used to improve the accuracy heat flux estimates. Hsieh et al. (1996) and Lloyd et al. (1991) showed that the free convection

formulation provides adequate estimates of heat flux even when friction velocities are not small.

In this chapter we show that errors associated with using this simple method of estimating heat and momentum fluxes has a relatively small effect on model estimates from dispersion models such as AERMOD. This study builds upon these earlier studies and those by Venkatram and Princevac (2008) and Qian et al. (2010) on determining the meteorological inputs for dispersion models under unstable conditions. Our approach to estimating surface fluxes modifies those presented earlier. The major contribution of this study is to examine the impact of using these inferred meteorological inputs on estimates of methane emissions from manure lagoons.

The next section focuses on the formulation and validation of a model to compute the metrological parameters required by dispersion models using reduced measurements. In the fourth section, the usefulness of the proposed method is evaluated by using the results in a dispersion model to infer methane emissions from a dairy manure lagoon system in Central California. The final section demonstrates an application of this method using a low-cost temperature sensor to measure temperature fluctuations.

4.3 Meteorological Model

4.3.1 Surface Flux Model

In this section we derive a semi-empirical formulation to compute the kinematic heat flux (Q_o) and surface friction velocity (u_*) (the momentum flux is $\rho_{air}u_*^2$; where ρ_{air} is the density of air) under unstable conditions using only measurements of horizontal wind speed

(U) and temperature fluctuations (σ_T) at a single level. Under unstable conditions, we can express the kinematic heat flux (Q_o) in terms of the standard deviation of the vertical wind speed (σ_w), and the standard deviation of the temperature (σ_T),

$$Q_o = r_{wT}\sigma_w\sigma_T \tag{4.1}$$

where, r_{wT}, is the correlation coefficient that, in principle is a function of z_r/L, where z_r is the height at which the heat flux is measured, and L is the Monin-Obukhov length give by,

$$L = -\frac{T_o u_*^3}{g\kappa Q_o} \tag{4.2}$$

where u_* is the friction velocity,g is the acceleration due to gravity, $\kappa(= 0.4)$ is the von Karman constant, and T_o is the reference temperature assumed to be the air temperature at the measurement height.

Equation (4.1) is the basis of the proposed method if r_{wT} varies little with z_r/L. The analysis of data, described later, indicates that this is a reasonable assumption (Section 4.3.2). Then, Q_0, can be estimated using measurements of the horizontal wind speed, U, and temperature fluctuations, σ_T using the formulations that follow.

The standard deviation of the vertical wind velocity, σ_w, is given by (Panofsky et al., 1977),

$$\sigma_w = 1.3u_*\left(1-\frac{z_r}{\kappa L}\right)^{\frac{1}{3}} \tag{4.3}$$

An equation that is alternative to Equation (4.3) is obtained by equating turbulence production in the surface layer to the dissipation rate,

$$\frac{u_*^3}{\kappa z_r}\phi_m\left(\frac{z_r}{L}\right)+\frac{g}{T_o}Q_o=\frac{\sigma_w^3}{L_d} \tag{4.4}$$

Where the left-hand side of the equation is the sum of the production of turbulence through shear and buoyancy respectively, and the right-hand side is a parameterization of the dissipation rate. The non-dimensional momentum function, $\phi_m(x)=(1-15x)^{-1/4}$ (Businger et al. 1971). Taking the dissipation scale, $L_d \sim z_r$, we get,

$$\sigma_w = 1.3u_*\left(\phi_m\left(\frac{z_r}{L}\right)-\frac{z_r}{L}\right)^{1/3} \tag{4.5}$$

Equations (4.3) and (4.5) yield similar results for σ_w (Figure 4-1) with Equation (4.3) performing slightly better especially when σ_w is large; thus, Equation (4.3) was used to compute σ_w in the subsequent analysis. Combining Equation (4.1) with Equation (4.3) yields the semi-empirical equation for the kinematic heat flux,

$$Q_o = 1.3r_{wT}\sigma_T u_*\left(1-\frac{z_r}{\kappa L}\right)^{\frac{1}{3}} \tag{4.6}$$

We will compare Equation (4.6) with a semi-empirical formulation suggested by Tillman (1972),

$$Q_o = 1.05\sigma_T u_* \left(0.05 - \frac{z_r}{L}\right)^{\frac{1}{3}} \tag{4.7}$$

Given the mean wind speed, U, and the standard deviation of temperature fluctuations, σ_T at some measurement height z_r, we can solve for Q_o and u_* using Equation (4.6), the expression for the Monin-Obukhov length, L (Equation (4.2)), and the friction velocity, u_* (Equation (4.8)).

The wind velocity profiles are modelled using Monin-Obukhov Similarity Theory (MOST) with the wind speed (U) at the measurement height of z_r related to the friction velocity, u_* by the following equation (Businger et al. 1971),

$$U(z_r) = \frac{u_*}{\kappa}\left[\ln\left(\frac{z_r - d_h}{z_o}\right) - \psi_m\ \zeta_1\ + \psi_m\ \zeta_o\ \right] \tag{4.8}$$

Where, d_h is the zero-plane displacement height, $\zeta_1 = (z_r - d_h)/L$, $\zeta_o = z_o/L$, and the function ψ_m is,

$$\psi_m\ \zeta\ = 2\ln\left(\frac{1+x'}{2}\right) + \ln\left(\frac{1+x'^2}{2}\right) - 2\tan^{-1}\ x'\ + \frac{\pi}{2} \tag{4.9}$$

for $Q_o > 0$, and $x' = (1 - 16\zeta)^{1/4}$.

In the next sub section, we describe the field studies used to collect the data that was used to evaluate the surface flux model.

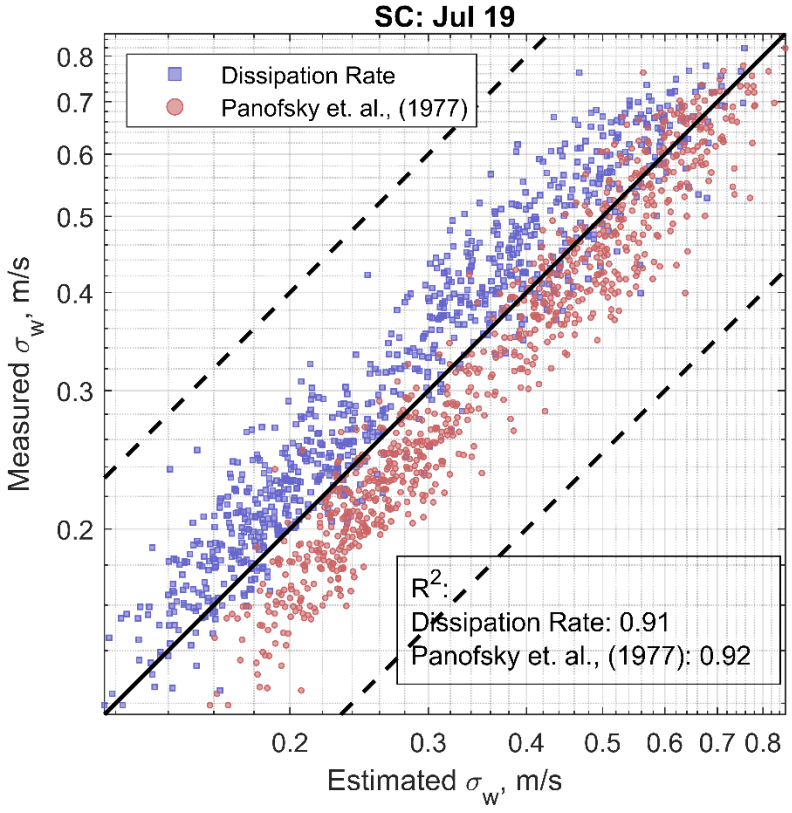

Figure 4-1 Comparison of σ_w predicted from the formulation by Panofsky et al., (1977) (Equation (4.3)) and from the dissipation rate (Equation (4.5))

4.3.2 Field Studies

Meteorological data used for the evaluation were collected at two locations. The first location was next to a manure lagoon in a dairy farm in Central California (CC). This site is surrounded by a cluster of dairy farms and can be classified as rural. Data was collected over three different seasons at this site. The second location was in the city of Riverside in Southern California (SC). This site was in a parking lot belonging to the University of California, Riverside. This site is located upwind of a freeway and can be classified as urban. The measurement periods at the two sites are tabulated in Table 4-1.

Table 4-1 Summary of meteorological data collected in Central California (CC) and Southern California (SC).

Location	Measurement Period	u_* (m/s)			Q_o $(K.m/s)$		
		Mean	**Min**	**Max**	**Mean**	**Min**	**Max**
CC	24-28 Mar 2019	0.14	0.01	0.41	0.05	0.01	0.22
CC	17-21 Jun 2019	0.18	0.04	0.38	0.09	0.01	0.23
CC	10-13 Sep 2019	0.14	0.03	0.31	0.08	0.01	0.25
SC	19-22 Jul 2019	0.23	0.03	0.61	0.10	0.01	0.40

The meteorological measurements were made using a 3-D Sonic Anemometer (CSAT3, Campbell Scientific) mounted between 2.3 to 2.4 m at the CC site during the different seasons and at 5 m at the SC Site. The sonic anemometer sampled data at a rate of 20 Hz. The sonic anemometer measures the wind speed along the three orthogonal directions and the air temperature (T). If u (along wind), v (crosswind), and w (vertical) are the velocity components along the three co-ordinate directions, the meteorological parameters were computed as follows,

Kinematic Heat Flux,

$$Q_o = \overline{w'T'} \tag{4.10}$$

Friction Velocity,

$$u_* = \left(\overline{w'u'}^2 + \overline{w'v'}^2\right)^{\frac{1}{4}} \tag{4.11}$$

where, $x' = \bar{x} - x$ denotes the turbulent or fluctuating component of the parameter of interest and $\bar{x}$ represents the mean of the parameter of interest over 5 minutes. Use of Equation (4.10) and (4.11) to compute Q_o and u_* requires the measurements of wind speed in 3-D and temperature.

The data was filtered for unstable conditions when $Q_0 > 0.01\ K.m/s$. Nighttime (1900 - 0500) unstable cases at the CC site were excluded as the stable periods mixed intermittently with unstable periods. Table 4-1 shows the statistics of the meteorological data collected at the two sites. The wind speeds were generally lower at the CC site than those at the SC site. At the SC site, the heat fluxes were always positive even after sunset possibly due to the advection of colder rural air onto the warmer urban surface.

The aerodynamic roughness length, z_o, at each site was estimated by assuming that the velocity profiles follow MOST. The roughness length, z_o is obtained by fitting the measured u_* (Equation (4.11)) with the similarity u_* (Qian et al. 2010) given by Equation (4.8). The zero-plane displacement, d_h was taken to be $5z_o$. A roughness length of 0.002 m and 0.15 m were obtained for the CC and the SC site respectively. The CC site has no buildings or any other large obstacles nearby while the SC site is in a parking lot surrounded by large buildings.

The kinematic heat flux (Q_o) and the product of the fluctuations in vertical wind speed and temperature $(\sigma_w.\sigma_T)$ computed using the full 3-D information from the sonic anemometer were highly correlated with the R^2 ranging from 0.84 to 0.93 (Figure 4-2). The slope of the

best fit line is the mean value of the correlation coefficient, r_{wT}. The value of r_{wT} ranged from 0.49 to 0.55 (Figure 4-2).

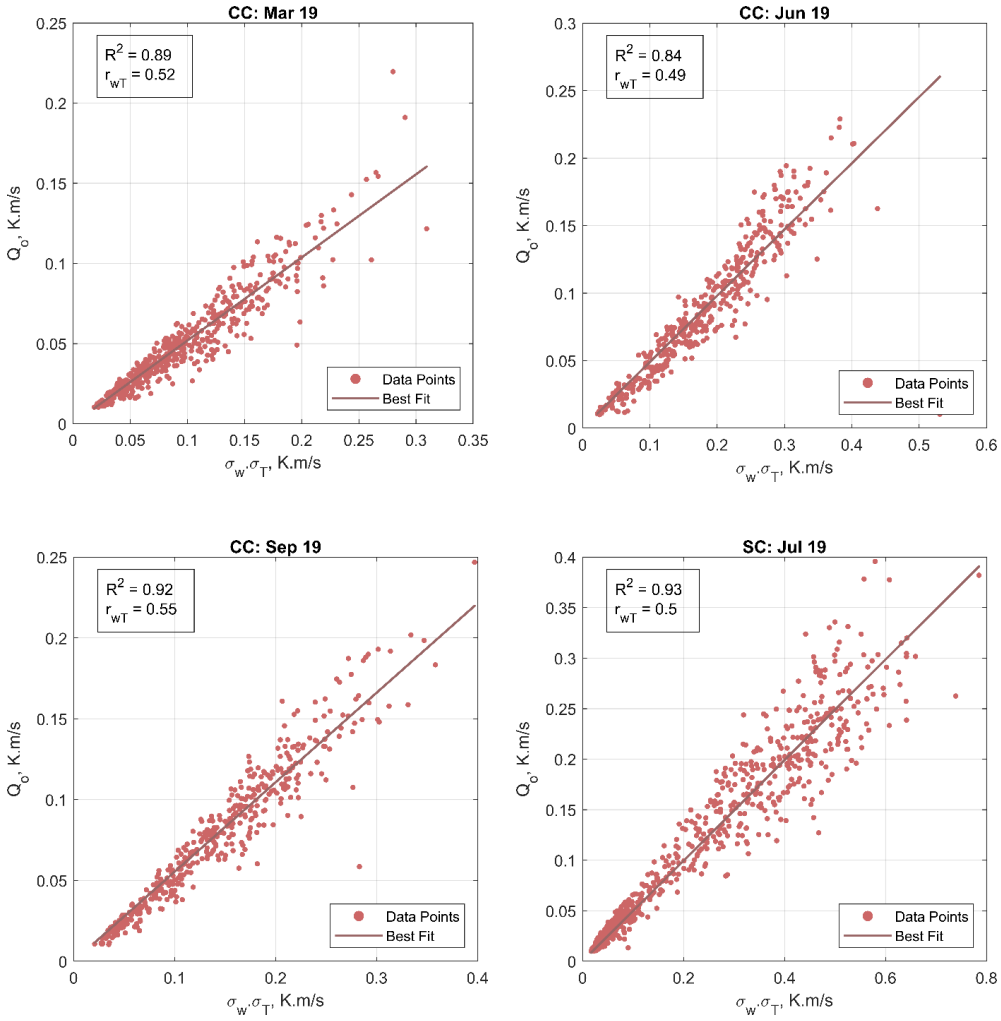

Figure 4-2 Scatter plot between the measured kinematic heat flux (Q_o) and the product of the fluctuations in the measured standard deviations of the vertical wind speed σ_w and temperature σ_T. The red dots are the observed data points, and the red line is the best fit line. The slope of the best fit line is r_{wT}.

The small variation of the slope of the best fit line over different seasons and sites suggests that a practical model for the heat flux can be based on a constant value of $r_{wT} = 0.5$,

ignoring its dependence on z_r/L (Figure 4-2). Thus, r_{wT} was considered a constant with a value of 0.5 in Equation (4.6).

In the next sub section, we evaluate this approach to compute heat flux using the data collected in the field studies described.

4.3.3 Evaluation with field studies

The heat flux model was evaluated using the meteorological data collected at the CC and the SC sites. The kinematic heat fluxes (Q_o) and the friction velocities(u_*) estimated with the heat flux model (Equation (4.2), (4.6), , and (4.8)) were compared with the measured values from the 3-D sonic anemometer (Equation (4.10) and (4.11)). The mean of the ratio of the estimated to the measured values (m_g) and the percentage of estimated values within a factor of 2 of the measured values $(fact2)$ were chosen as the primary measures of model performance. The m_g quantifies the overall bias in the model with values greater than 1 indicating overestimates and values less than 1 indicating underestimates.

Comparison of estimates of Q_o and u_* based on Equation (4.7), suggested by Tillman (1972), with Equation (4.6) based on the constant correlation used in this study show that both the models estimate u_* very well, but Equation (4.7) tends to overestimate Q_o with an m_g of 1.59 (Figure 4-3). Thus, Equation (4.7) improves the heat flux model.

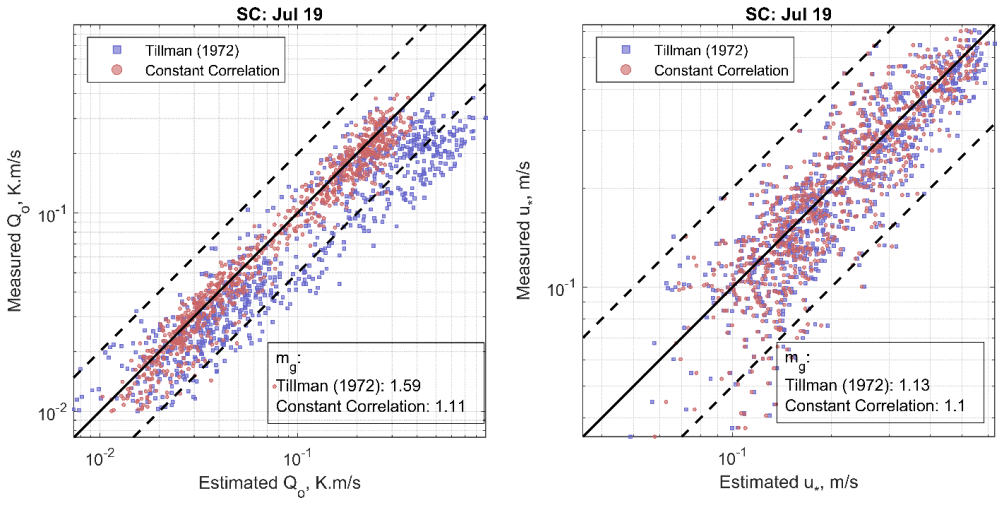

Figure 4-3 Comparison of the formulation by Tillman (1972) (Equation (4.7); Blue Squares) with the constant correlation formulation (Equation (4.6); Red Circles) in estimating the kinematic heat flux, Q_o (left) and the surface friction velocity, u_* (right) from the data collected at the Southern California site. The formulation by Tillman (1972) overestimates Q_o.

The flux model was able to estimate the kinematic heat fluxes, Q_o very well over all the measured seasons and sites (Figure 4-4). The m_g between the estimated and measured Q_o ranged between 1.09 and 1.35. There was a slight overestimating at the CC site in June with a m_g of 1.35. More than 95% of the estimated fluxes lie within a factor of 2 of the measured fluxes.

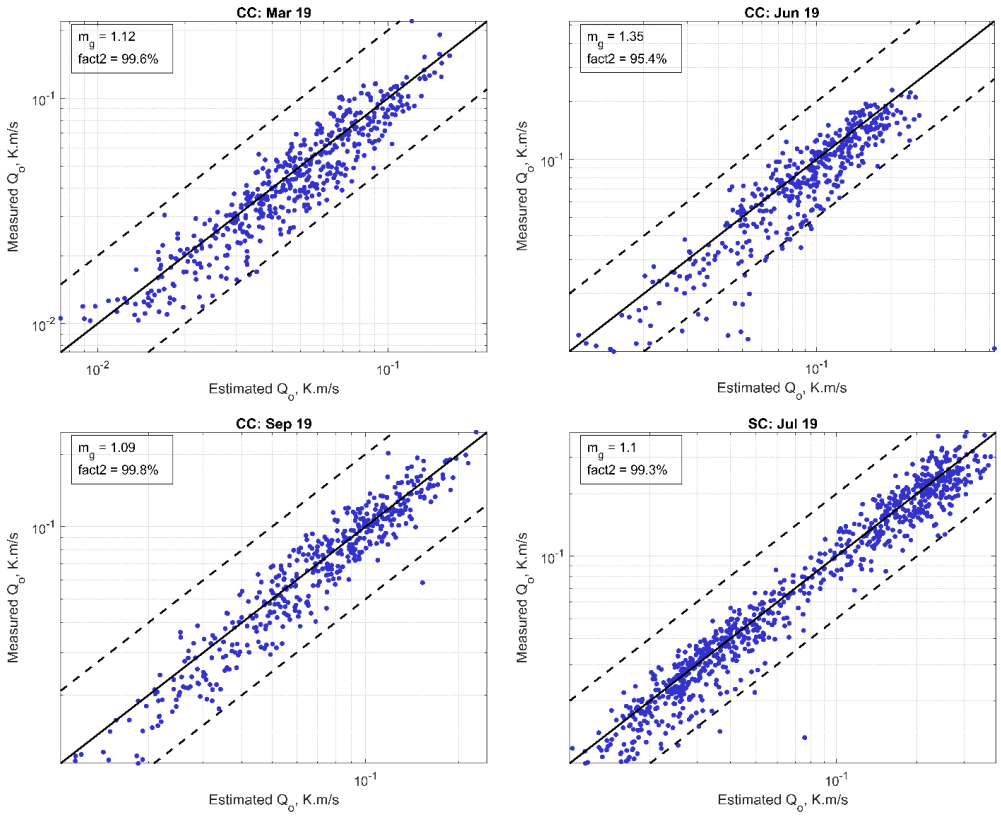

Figure 4-4 Scatter plot between the measured and estimated kinematic heat fluxes (Q_o). The dashed lines next to the solid 1:1 line enclose the estimated values within a factor of 2 of the measured values.

The measured friction velocities agreed very well with the modeled values (Figure 4-5). The m_g ranged from 1.06 to 1.11 indicating very little positive bias in the model. The higher scatter at the CC site compared to that at the SC site suggests that the wind profiles follow MOST better at the SC site than at the CC site (Figure 4-5). The percentage of estimated values within a factor of 2 of the measured values at the CC and SC site ranged between 85.8% – 95.9%.

The next section examines the performance of this simple model for computing heat flux by applying a dispersion model to infer methane emissions from manure lagoons located at a dairy in Central California (CC).

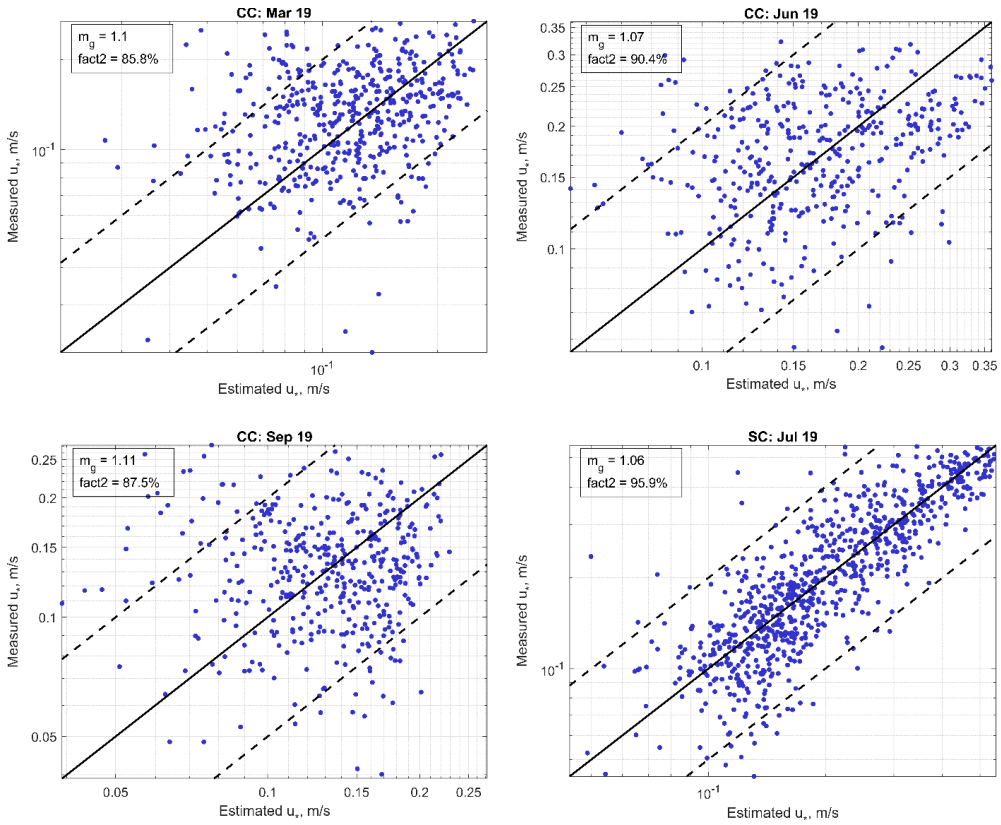

Figure 4-5 Scatter plot between the measured and estimated friction velocities (u_*). The dashed lines next to the solid 1:1 line enclose the estimated values within a factor of 2 of the measured values.

4.4 Estimating methane emissions

Methane mixing ratio measurements were made with simultaneous meteorological measurements near the manure lagoons in the dairy at the CC site. Measurements of methane were conducted with an instrumented mobile platform that stopped at various locations around the lagoons for about 9 minutes at each location. Atmospheric methane ratios were collected with a cavity ring-down spectrometer (Picarro 2210-i) at a height of 2.87 m AGL. More details on the measurement system can be found in Thiruvenkatachari et al., (2020).

The measurements were made in field studies conducted during four different seasons: 25th and 30th of March 2019, 18th and 19th of June 2019, 10th and 11th of September 2019, and 16th of January 2020. A dispersion model based on the numerical solution of the two-dimensional advection-diffusion equation (Thiruvenkatachari et al. 2020), was used to infer emissions from the lagoons. The model, which requires micrometeorological inputs to construct vertical profiles of wind speeds and eddy diffusivities, has been evaluated with data from the Prairie Grass experiment (Barad 1958; Nieuwstadt and van Ulden 1978a) and the Idaho Falls study (Finn et al. 2010).

The dispersion model treats the manure lagoon as an area source. The contribution of the area source to the concentration at a receptor is the integral of the contributions from a set of line sources perpendicular to the wind direction. The analytical solution formulated in Venkatram and Horst, (2006) provides the horizontal concentration distribution from each line source.

The measured atmospheric methane concentration (mixing ratio) measured at any receptor $'j'$ is related to the corresponding model estimate as follows,

$$C_j = C_b + \sum_i E_i T_{ij} + \varepsilon_j \tag{4.12}$$

where T_{ij} is the transport coefficient which is the modeled impact of source $'i'$on receptor $'j'$ using a unit emission rate, E_i is the unknown emission rate from source $'i'$, and ε_j is the residual. The background concentration, C_b is also treated as an unknown. The emission

rates and the background concentration are the values that minimize $\sum_j \varepsilon_j^2$ with the constraint that their values are greater than or equal to zero.

The 95% confidence intervals were computed through a version of bootstrapping that adds residuals between the observed and estimated concentrations to model estimates to create pseudo-observations. These observations are then used in Equation (4.12) to derive emission estimates corresponding to 1000 sets of pseudo-observations. The bootstrapping includes residuals from the application of the dispersion model to analyze data from all the field studies conducted at the site.

The emission rates of the manure lagoon and their confidence intervals inferred from the dispersion model using the measured (3-D information from the sonic anemometer) and the modelled (heat flux model) meteorological inputs show that the differences in the mean emission rates are much smaller than the model uncertainty (Figure 4-6). These results suggest that the measured and the modelled meteorological inputs can be used interchangeably.

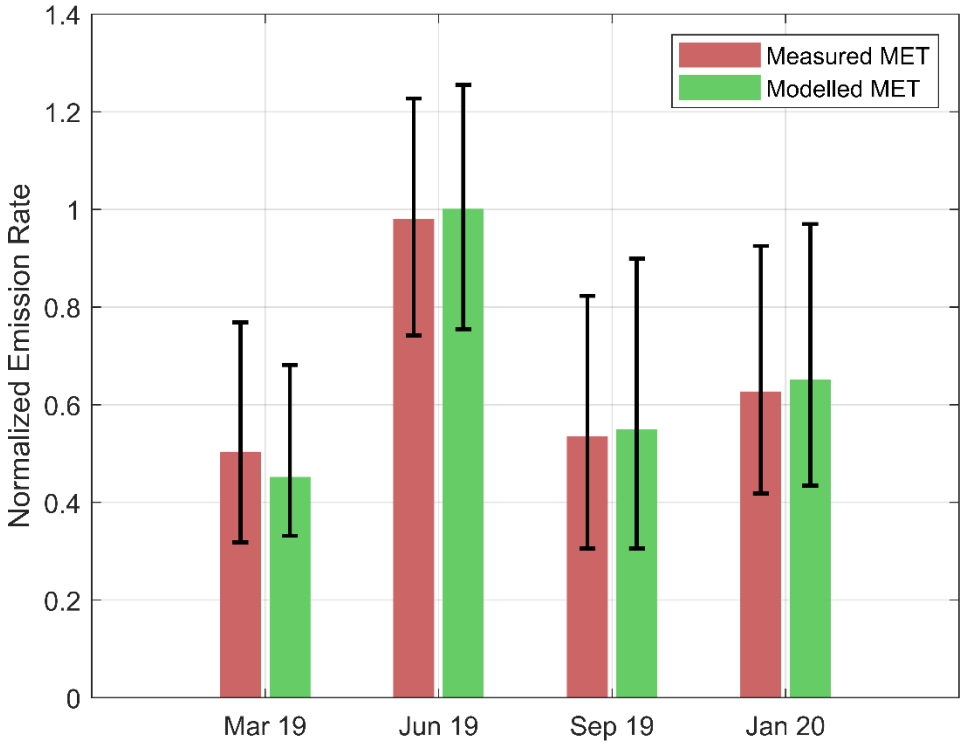

Figure 4-6 Emission rates and their 95% confidence intervals from the manure lagoons inferred from the dispersion model using the measured (red) and modelled (green) meteorological inputs. The differences in the mean emission rates are much lower than the model uncertainty.

Estimating the roughness length, z_o requires knowledge of both u_* and Q_o and thus cannot be computed when only the measurements of temperature fluctuations and horizontal wind speeds are available (Section 4.3.2). The sensitivity of the emission estimates to uncertainty in z_o was examined by using meteorological inputs corresponding to roughness lengths ranging from an order of magnitude lower to an order of magnitude higher than the best estimate ($z_o = 0.002\ m$). The differences in the emission rates caused by the uncertainty in z_o were well within the uncertainty of the model estimates (Figure 4-7).

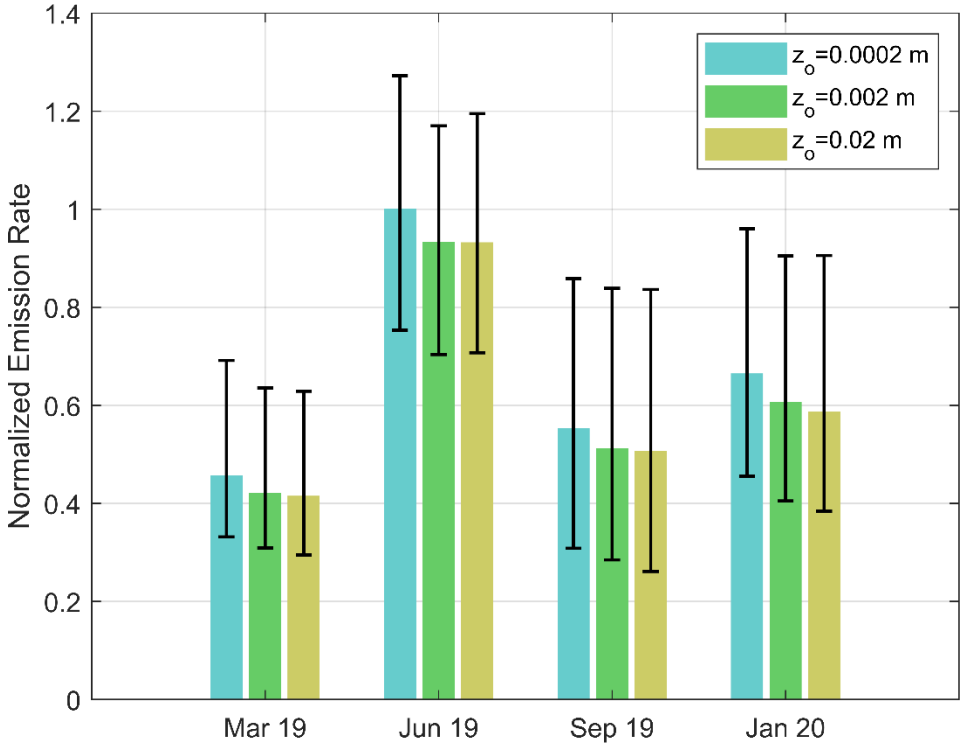

Figure 4-7 Bar chart showing the sensitivity of the emission estimates to the roughness length, z_o. The difference in the emission estimates due to z_o are much lower than the model uncertainty.

4.5 Performance with a low-cost temperature sensor

In this section we demonstrate the usefulness of the surface flux model by using a low-cost sensor rather than a 3-D sonic anemometer to measure temperature fluctuations. This method can be the basis for making on-site estimates of micrometeorological inputs with instrumentation that can be easily installed in a mobile laboratory.

Measurements of horizontal wind speed and temperature were made at the University of California Riverside Engineering Center for Environmental Research and Technology (CE-CERT) between January 10th to 13th, 2022 with a 3-D sonic anemometer (CSAT3, Campbell Scientific) collocated with a bead thermistor (iMET-XQ2, InterMet) at a height

of 1.5 m (Figure 4-8). The sonic anemometer sampled 3-D wind speeds and temperature at a frequency of 20 Hz, while the thermistor measured the temperature, atmospheric pressure, and humidity at a frequency of 1 Hz.

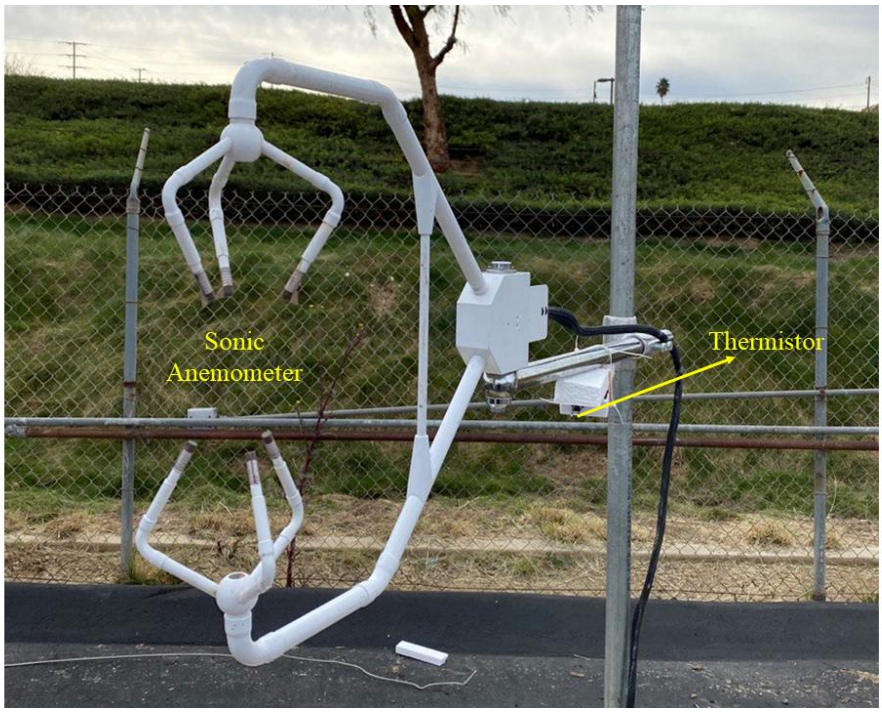

Figure 4-8 Picture showing the experimental setup used to measure the horizontal wind speeds and temperature. A 3-D sonic anemometer was collocated with a bead thermistor.

The temperature fluctuations (σ_T) measured by the thermistor are well correlated with the σ_T measured by the sonic anemometer with a correlation coefficient of 0.8 (Figure 4-9). But the σ_T from the thermistor was on an average 0.7 times that from the sonic anemometer. Since no pollutant concentrations were measured during this experiment, we determined the usefulness of the σ_T measured by the thermistor by repeating the exercise performed in Section 4.4 by relating the temperature fluctuations measured with the onsite sonic

anemometer to the possible measurements from the thermistor using the regression equation (Figure 4-9),

$$\sigma_T \ XQ2 \ = 0.66\sigma_T \ CSAT3 \ + 0.02 + \in \tag{4.13}$$

where $\sigma_T(XQ2)$ is the modelled thermistor temperature fluctuation, $\sigma_T(CSAT3)$ is the measured sonic anemometer temperature fluctuation and ϵ is a normally distributed random number corresponding to the deviations between the sonic anemometer and thermistor σ_T measurements shown in Figure 4-9. This allowed us to use the simulated thermistor temperature fluctuations in the heat flux model to determine meteorological inputs for the dispersion model. We generated 100 sets of modelled meteorological inputs using Equation (4.13) which were then used to determine the mean and the 95% confidence interval of the methane emission rates. This confidence limit represents the sensitivity of the emission rates to uncertainty in σ_T.

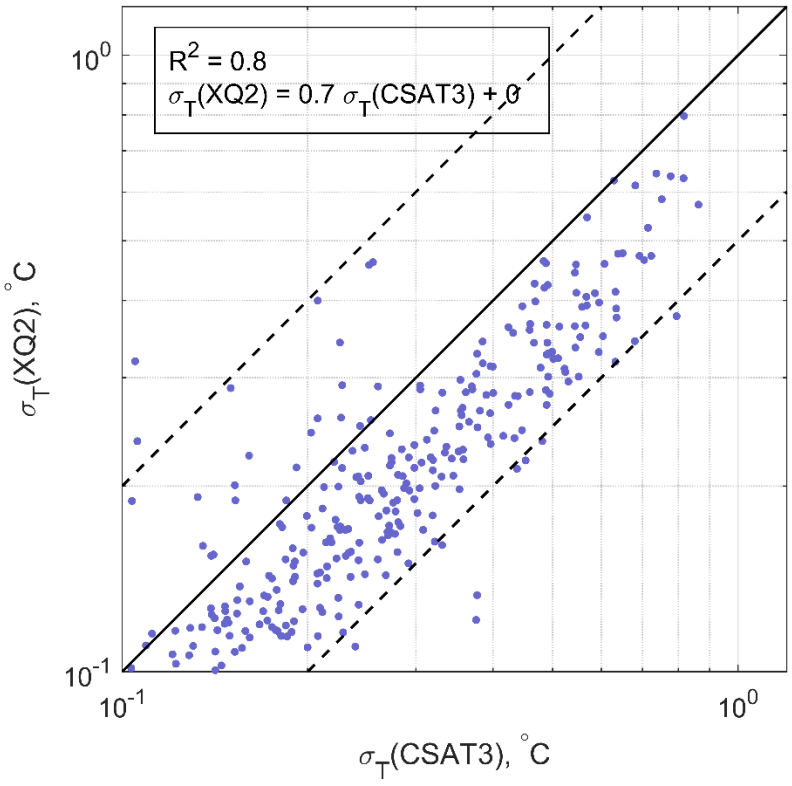

Figure 4-9 Scatter plot between the σ_T measured by the sonic anemometer (CSAT3) and the thermistor (XQ2). The thermistor σ_T is 0.7 times the sonic anemometer σ_T.

The measured and the modelled meteorological inputs were then used in the dispersion model along with the methane mixing ratio measurements described in the last section to infer the methane emission rates. The differences in the mean methane emission rates are much less than the uncertainty in the inferred emission rates (Figure 4-10). Also, the uncertainty in the emission rates due to the uncertainties in the measured σ_T was much lower than the uncertainty inherent in the modelling process. These results suggest that measurements from a low-cost temperature can be used in the heat flux model to obtain useful estimates of meteorological inputs needed for dispersion models.

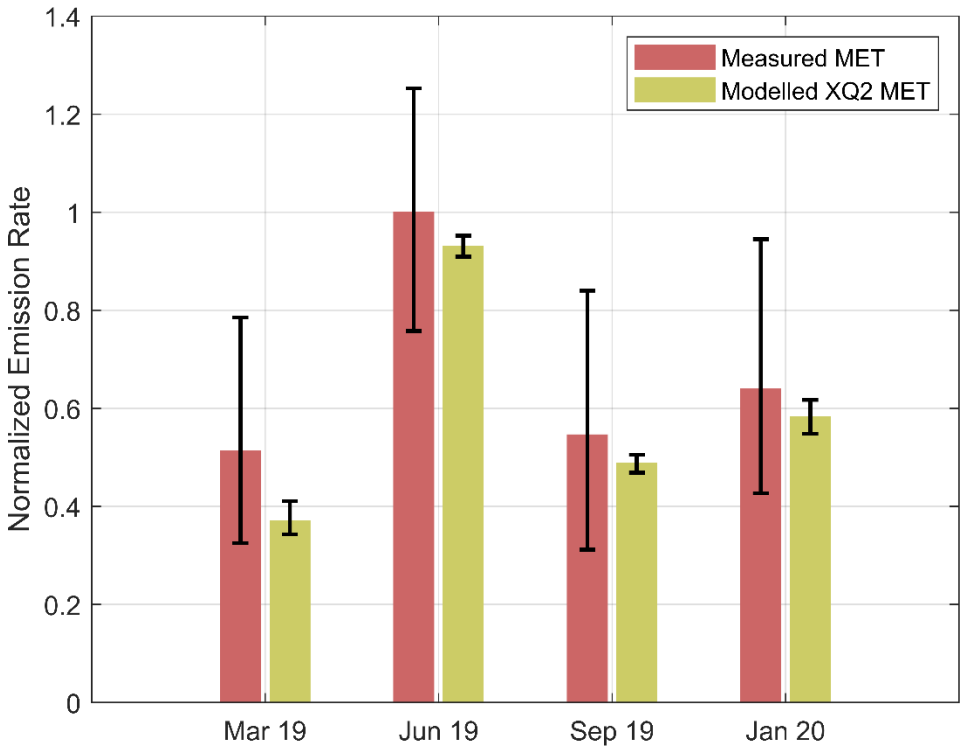

Figure 4-10 Bar graph showing the emission rate estimated by the dispersion model and their 95% confidence interval using the measured meteorology (left, red) and the modelled meteorology (right, yellow) using temperature fluctuations from the thermistor. The uncertainty inherent in the modelling process is much higher than the uncertainty due to the measured σ_T.

5 Conclusion

In this dissertation, I have demonstrated two applications of dispersion models. In the first, I used a dispersion model to estimate emissions of methane, an important green-house gas, from manure lagoons in dairy farms. In the second application, I used a dispersion model to interpret data collected from a field study designed to examine the impact of near-road noise barriers on dispersion of vehicular emissions from freeways

As part these studies, I developed and evaluated a micrometeorological model to estimate the meteorological inputs required by dispersion models. This model obviates the need for measurements with 3-D sonic anemometers, which are usually used for on-site measurements of micrometeorology. We will discuss the major impacts of each of these studies separately in the following sections.

5.1 Estimating methane emissions from dairy manure lagoons using dispersion models

A widely used method to estimate emissions from area sources, such as manure lagoons, is based on using a dispersion model, such as WindTrax, to relate emissions to concentration measurements made in the vicinity of the source. The uncertainty associated with such emission estimates depends on uncertainties in 1) the formulation of the dispersion model used to infer emissions, 2) model inputs that include micrometeorology, physical characteristics of the source, and locations of concentration measurements, and 3) the duration and accuracy of concentration measurements used to infer emissions.

We have demonstrated a new sampling and modelling approach to estimating emissions from manure lagoons. The approach also provides the uncertainty associated with these emission estimates. Our approach to infer emissions from lagoons has the following advantages over methods used in previous studies: (1) it is easily deployed and applicable to other gases if they are measured, (2) it enables separate emission estimates for different sectors of the manure management system either by separating a single pond into areas with different emission rates as in the Southern California dairy, or by isolating different treatment lagoons as in the Central California dairy, (3) it provides uncertainty estimates for emissions, and (4) it does not require a measurement of background methane concentrations as the background is a parameter fitted in the model. However, as with most techniques to estimate lagoon emissions, site access is required.

I applied the sampling and modeling approach to infer methane emissions at two dairies, one in Southern California and the other in Central California. The results show that the differences in the formulation of the models used to infer emissions can result in emission estimates that can differ by as much as a factor of two. The uncertainty in emission estimates from any one model ranges from 0.8 times to 1.4 times the best fit value. These uncertainty estimates, which are specific to the field studies considered in this paper, are the result of a combination of factors. There is a need for future studies to examine the relative roles of these factors in determining total uncertainty. This information is critical to determining the efficacy of manure management methods to mitigate methane emissions from manure ponds.

In principle, this technique can be applied to any emission source of a similar scale and surface expression. Emission estimates for the two farms given here double the number of methane emission estimates for California dairy lagoons (Arndt et al. 2018), and if deployed more widely have a potential to fill in key gaps in our understanding of the variability of methane emissions from this source. Because it is rapidly deployable, the technique can be used across multiple times of days and seasons to examine the role of temporal drivers of emissions.

5.2 Impacts of Noise Barriers on Near-road Air Quality

I played a major role in the first tracer study designed to examine the mitigating effect of noise barriers under real-world conditions. The data collected from the field study will be used by regulatory agencies, such as the US Environmental Protection Agency, to evaluate dispersion models that incorporate the effects of solid near-road barriers.

I analyzed the data using a dispersion model that incorporated the major processes responsible for the mitigating impact of a barrier: lifting of the plume above the barrier followed by entrainment of the elevated plume into the wake of the barrier. The model provided an adequate description of the measured concentrations except when the wind speeds were less than 1 m/s: the model overestimated measured concentrations by a factor of three. We proposed an approach to reducing this overestimation through a function that depends on the upwind friction velocity.

An examination of the data showed that the downwind variation of the tracer concentration is consistent with the results from the simple model described by Equation (3.16). This

model is based on the idea that the mitigating effect of a sound barrier on near-road air quality is equivalent to shifting the source, the road, by the height of the barrier divided by the upwind turbulent intensity. This equation is a rule-of-thumb for estimating the impact of a sound barrier as a function of distance from a road.

5.3 Estimating Micrometeorological Inputs for Dispersion Models

In this study the micrometeorological inputs required by dispersion models, such as AERMOD, were estimated with a model that uses the horizontal wind speed and temperature fluctuations at a single level. The model was evaluated using field measurements from 3-D sonic anemometers at sites in Central California and Southern California. The impact of the deviations of the modeled from the measured meteorological inputs were evaluated by comparing methane emissions inferred from a dispersion model based on the two sets of inputs. The differences in the mean emission estimates are much smaller than the uncertainties in the emission estimates. The uncertainty in roughness lengths had little impact on the emission estimates.

We show that the proposed method does not have to have to rely on measurements from a 3-D sonic anemometer to measure temperature fluctuations required for the method described here. A low-cost temperature sensor provides useful estimates. This suggests that any instruments that can measure horizonal winds and temperature fluctuations can be used to determine meteorological inputs for dispersion models used to estimate emissions from area sources such as manure lagoons. Such instruments can be carried on mobile platforms

or even unmanned aerial vehicles to provide meteorological inputs quickly and in locations where it is difficult to set up a 3-D sonic anemometer.

REFERENCES

A. A. M. Holtslag, Ulden AP Van (1985) Estimation of Atmospheric Boundary Layer Parameters for Diffusion Applications. J Clim Appl Meterology

Ahangar F, Freedman F, Venkatram A (2019) Using Low-Cost Air Quality Sensor Networks to Improve the Spatial and Temporal Resolution of Concentration Maps. Int J Environ Res Public Health 16:1252. https://doi.org/10.3390/ijerph16071252

Albertson JD, Parlange MB, Katul GG, et al (1995) Sensible Heat Flux From Arid Regions: A Simple Flux-Variance Method. Water Resour Res 31:969–973. https://doi.org/10.1029/94WR02978

Amini S, Ahangar FE, Schulte N, Venkatram A (2016) Using models to interpret the impact of roadside barriers on near-road air quality. Atmos Environ 138:55–64. https://doi.org/10.1016/j.atmosenv.2016.05.001

Amini S, Kuwayama T, Gong L, et al (2022) Evaluating California dairy methane emission factors using short-term ground-level and airborne measurements. Atmos Environ X 14:100171. https://doi.org/10.1016/j.aeaoa.2022.100171

Appel KW, Bash JO, Fahey KM, et al (2021) The Community Multiscale Air Quality (CMAQ) model versions 5.3 and 5.3.1: system updates and evaluation. Geosci Model Dev 14:2867–2897. https://doi.org/10.5194/gmd-14-2867-2021

Arndt C, Leytem AB, Hristov AN, et al (2018) Short-term methane emissions from 2 dairy farms in California estimated by different measurement techniques and US Environmental Protection Agency inventory methodology: A case study. J Dairy Sci 101:11461–11479. https://doi.org/10.3168/jds.2017-13881

Baldauf R, Thoma E, Khlystov A, et al (2008) Impacts of noise barriers on near-road air quality. Atmos Environ 42:7502–7507. https://doi.org/10.1016/j.atmosenv.2008.05.051

Baldé H, VanderZaag AC, Burtt S, et al (2016) Measured versus modeled methane emissions from separated liquid dairy manure show large model underestimates. Agric Ecosyst Environ 230:261–270. https://doi.org/10.1016/j.agee.2016.06.016

Barad ML (1958) Project prairie grass, a field program in diffusion. Volume 1 (no. Grp-59-vol-1). Air Force Cambridge Res Labs Hanscom AFB MA. https://doi.org/10.1016/0022-460X(71)90105-2

Bonifacio HF, Maghirang RG, Razote EB, et al (2013) Comparison of AERMOD and WindTrax dispersion models in determining PM10 emission rates from a beef cattle feedlot. J Air Waste Manag Assoc 63:545–556. https://doi.org/10.1080/10962247.2013.768311

Brandt S, Perez L, Künzli N, et al (2014) Cost of near-roadway and regional air pollution–attributable childhood asthma in Los Angeles County. J Allergy Clin Immunol

134:1028–1035. https://doi.org/10.1016/j.jaci.2014.09.029

Brantley HL, Thoma ED, Squier WC, et al (2014) Assessment of methane emissions from oil and gas production pads using mobile measurements. Environ Sci Technol 48:14508–14515. https://doi.org/10.1021/es503070q

Bucholtz S, Donaldson K, England S, et al (2011) American Housing Survey for Selected Metropolitan Areas : 2009

Bühler M, Häni C, Ammann C, et al (2022) Using the inverse dispersion method to determine methane emissions from biogas plants and wastewater treatment plants with complex source configurations. Atmos Environ X 13:100161. https://doi.org/10.1016/j.aeaoa.2022.100161

Businger JA, Wyngaard JC, Izumi Y, Bradley EF (1971) Flux-Profile Relationships in the Atmospheric Surface Layer. J Atmos Sci 28:181–189. https://doi.org/10.1175/1520-0469(1971)028<0181:FPRITA>2.0.CO;2

CARB (2019) Greenhouse Gas Emission Inventory - Query Tool for years 2000 to 2016 (11th Edition). https://www.arb.ca.gov/app/ghg/2000_2016/ghg_sector.php. Accessed 10 Apr 2019

Carruthers DJ, Seaton MD, McHugh CA, et al (2011) Comparison of the complex terrain algorithms incorporated into two commonly used local-scale air pollution dispersion models (ADMS and AERMOD) using a hybrid model. J Air Waste Manag Assoc 61:1227–1235. https://doi.org/10.1080/10473289.2011.609750

Chen Z, Newgard CB, Kim JS, et al (2019) Near-roadway air pollution exposure and altered fatty acid oxidation among adolescents and young adults – The interplay with obesity. Environ Int 130:104935. https://doi.org/10.1016/j.envint.2019.104935

Cimorelli AJ, Perry SG, Venkatram A, et al (2005) AERMOD: A dispersion model for industrial source applications. Part I: General model formulation and boundary layer characterization. J Appl Meteorol 44:. https://doi.org/10.1175/JAM2227.1

Eckman RM (1994) Re-examination of empirically derived formulas for horizontal diffusion from surface sources. Atmos Environ 28:265–272. https://doi.org/10.1016/1352-2310(94)90101-5

Faulkner WB, Powell JJ, Lange JM, et al (2007) C d m a e g l a s. 50:2189–2197

Finn D, Clawson KL, Carter RG, et al (2010) Tracer studies to characterize the effects of roadside noise barriers on near-road pollutant dispersion under varying atmospheric stability conditions. Atmos Environ 44:204–214. https://doi.org/10.1016/j.atmosenv.2009.10.012

Flesch TK, Wilson JD, Harper LA, Crenna BP (2005) Estimating gas emissions from a farm with an inverse-dispersion technique. Atmos Environ 39:4863–4874. https://doi.org/10.1016/j.atmosenv.2005.04.032

Flesch TK, Wilson JD, Yee E (1995) Backward-time Lagrangian stochastic dispersion models and their application to estimate gaseous emissions. J. Appl. Meteorol. 34:1320–1332

Grant RH, Boehm MT, Lawrence AF (2013) Comparison of a backward-Lagrangian stochastic and vertical radial plume mapping methods for estimating animal waste lagoon emissions. Agric For Meteorol 180:236–248. https://doi.org/10.1016/j.agrformet.2013.06.013

Grell GA, Peckham SE, Schmitz R, et al (2005) Fully coupled "online" chemistry within the WRF model. Atmos Environ 39:6957–6975. https://doi.org/10.1016/j.atmosenv.2005.04.027

Hagler GSW, Tang W, Freeman MJ, et al (2011) Model evaluation of roadside barrier impact on near-road air pollution. Atmos Environ 45:2522–2530. https://doi.org/10.1016/j.atmosenv.2011.02.030

Heist DK, Perry SG, Brixey LA (2009) A wind tunnel study of the effect of roadway configurations on the dispersion of traffic-related pollution. Atmos Environ 43:5101–5111. https://doi.org/10.1016/j.atmosenv.2009.06.034

Hopkins FM, Ehleringer JR, Bush SE, et al (2016) Mitigation of methane emissions in cities: How new measurements and partnerships can contribute to emissions reduction strategies. Earth's Futur 4:408–425. https://doi.org/10.1002/2016EF000381

Hristov AN, Harper M, Meinen R, et al (2017) Discrepancies and Uncertainties in Bottom-up Gridded Inventories of Livestock Methane Emissions for the Contiguous United States. Environ Sci Technol 51:13668–13677. https://doi.org/10.1021/acs.est.7b03332

Hsieh CI, Katul GG, Schieldge J, et al (1996) Estimation of momentum and heat fluxes using dissipation and flux- variance methods in the unstable surface layer. Water Resour Res 32:2453–2462. https://doi.org/10.1029/96WR01337

Isakov V, Venkatram A, Touma JS, et al (2007) Evaluating the use of outputs from comprehensive meteorological models in air quality modeling applications. Atmos Environ 41:. https://doi.org/10.1016/j.atmosenv.2006.10.043

Kaharabata SK, Schuepp PH, Desjardins RL (2000) Source strength determination of a tracer gas using an approximate solution to the advection-diffusion equation for microplots. Atmos Environ 34:2343–2350

Kia S, Flesch TK, Freeman BS, Aliabadi AA (2022) Calculating gas emissions from open-pit mines using inverse dispersion modelling: A numerical evaluation using CALPUFF and CFD-LS. J Wind Eng Ind Aerodyn 226:105046. https://doi.org/10.1016/j.jweia.2022.105046

Lawson CL, Hanson RJ (1974) Solving Least Square Problems. Prentice-Hall

Leytem AB, Bjorneberg DL, Koehn AC, et al (2017) Methane emissions from dairy lagoons in the western United States. J Dairy Sci 100:6785–6803. https://doi.org/10.3168/jds.2017-12777

Lloyd CR, Culf AD, Dolman AJ, Gash JHC (1991) Estimates of sensible heat flux from observations of temperature fluctuations. Boundary-Layer Meteorol 57:311–322. https://doi.org/10.1007/BF00120051

Mangino J, Bartram D, Brazy A (2002) Development of a methane conversion factor to estimate emissions from animal waste lagoons. 11th Int Emiss Invent Conf

McGinn SM (2013) Developments in micrometeorological methods for methane measurements. Animal 7 Suppl 2:386–393. https://doi.org/10.1017/S1751731113000657

Monin AS, Yaglom AM (1971) Statistical Fluid Mechanics. Volume 1. Mechanics of Turbulence. MIT Press, Cambridge

Mooney CJ, Wilson JD (1993) Disagreements between gradient-diffusion and Lagrangian stochastic dispersion models, even for sources near the ground. Boundary-Layer Meteorol 64:291–296. https://doi.org/10.1007/BF00708967

National Academies of Sciences, Engineering and M (2018) Improving Characterization of Anthropogenic Methane Emissions in the United States

Nieuwstadt FTM, van Ulden AP (1978a) A numerical study on the vertical dispersion of passive contaminants from a continuous source in the atmospheric surface layer. Atmos Environ 12:2119–2124. https://doi.org/10.1016/0004-6981(78)90166-X

Nieuwstadt FTM, van Ulden AP (1978b) A numerical study of the vertical dispersion of passive contaminants from a continuous source in the atmospheric surface layer. Atmos Environ 14:267–269. https://doi.org/https://doi.org/10.1016/0004-6981(78)90166-X

Nieuwstadt TM, Ulden AP Van (1978) A numerical study on the vertical dispersion of passive contaminants from a continuous source in the atmospheric surface layer. Atmos Environ 14:267–269. https://doi.org/https://doi.org/10.1016/0004-6981(78)90166-X

Olesen HR, Berkowicz R, Løfstrøm P (2007) OML: Review of model formulation

Panofsky HA, Tennekes H, Lenschow DH, Wyngaard JC (1977) The characteristics of turbulent velocity components in the surface layer under convective conditions. Boundary-Layer Meteorol 11:355–361. https://doi.org/10.1007/BF02186086

Pineda Rojas AL (2014) Simple atmospheric dispersion model to estimate hourly ground-level nitrogen dioxide and ozone concentrations at urban scale. Environ Model Softw 59:127–134. https://doi.org/10.1016/j.envsoft.2014.05.016

Pournazeri S, Princevac M (2015) Sound wall barriers: Near roadway dispersion under neutrally stratified boundary layer. Transp Res Part D Transp Environ 41:386–400. https://doi.org/10.1016/j.trd.2015.09.025

Qian W, Princevac M, Venkatram A (2010) Using temperature fluctuation measurements to estimate meteorological inputs for modelling dispersion during convective conditions in urban areas. Boundary-Layer Meteorol 135:269–289. https://doi.org/10.1007/s10546-010-9479-y

Ro KS, Johnson MH, Stone KC, et al (2013) Measuring gas emissions from animal waste lagoons with an inverse-dispersion technique. Atmos Environ 66:101–106. https://doi.org/10.1016/j.atmosenv.2012.02.059

Saunois M, Bousquet P, Poulter B, et al (2016a) The global methane budget 2000-2012. Earth Syst Sci Data 8:697–751. https://doi.org/10.5194/essd-8-697-2016

Saunois M, Jackson RB, Bousquet P, et al (2016b) The growing role of methane in anthropogenic climate change. Environ Res Lett 11:. https://doi.org/10.1088/1748-9326/11/12/120207

Sawford B (2001) Project Prairie Grass—a classic atmospheric dispersion experiment revisited. 14th Aust fluid mech Conf 175–178

Schulte N, Snyder M, Isakov V, et al (2014) Effects of solid barriers on dispersion of roadway emissions. Atmos Environ 97:286–295. https://doi.org/10.1016/j.atmosenv.2014.08.026

Scire JS, Strimaitis DG, Yamartino RJ (1990) Model Formulation and User's Guide for the CALPUFF Dispersion Model. Eearth Tech Inc 310

Snyder MG, Venkatram A, Heist DK, et al (2013) RLINE: A line source dispersion model for near-surface releases. Atmos Environ 77:748–756. https://doi.org/10.1016/j.atmosenv.2013.05.074

Thiruvenkatachari RR, Carranza V, Ahangar F, et al (2020) Uncertainty in using dispersion models to estimate methane emissions from manure lagoons in dairies. Agric For Meteorol 290:108011. https://doi.org/10.1016/j.agrformet.2020.108011

Tillman JE (1972) The Indirect Determination of Stability, Heat and Momentum Fluxes in the Atmospheric Boundary Layer from Simple Scalar Variables During Dry Unstable Conditions. J Appl Meteorol 11:783–792. https://doi.org/10.1175/1520-0450(1972)011<0783:TIDOSH>2.0.CO;2

Todd RW, Cole NA, Casey KD, et al (2011) Methane emissions from southern High Plains dairy wastewater lagoons in the summer. Anim Feed Sci Technol 166–167:575–580. https://doi.org/10.1016/j.anifeedsci.2011.04.040

Touma JS, Isakov V, Cimorelli AJ, et al (2007) Using prognostic model-generated meteorological output in the AERMOD dispersion model: An illustrative application

in Philadelphia, PA. J. Air Waste Manag. Assoc. 57:586–595

United Nations Environment Programme and Climate and Clean Air Coalition (2021) Global Methane Assessment: Benefits and Costs of Mitigating Methane Emissions. Nairobi

US Environmental Protection Agency (1990) Inventory of U.S. Greenhouse Gas Emissions and Sinks: 1990-2014 – Main Text. 1–558

USEPA (2015) Transportation and Climate Division Office of Transportation and Air Quality U.S. Environmental Protection Agency. Transportation Conformity Guidance for Quantitative Hot-spot Analyses in PM 2.5 and PM 10 Nonattainment and Maintenance Areas. EPA-420-B-15-084

van Ulden AP (1978) Simple estimates for vertical diffusion from sources near the ground. Atmos Environ 12:2125–2129. https://doi.org/10.1016/0004-6981(78)90167-1

Venkatram A (1992) Vertical dispersion of ground-level releases in the surface boundary layer. Atmos Environ Part A, Gen Top 26:. https://doi.org/10.1016/0960-1686(92)90253-H

Venkatram A, Horst TW (2006) Approximating dispersion from a finite line source. Atmos Environ 40:2401–2408. https://doi.org/10.1016/j.atmosenv.2005.12.014

Venkatram A, Princevac M (2008) Using measurements in urban areas to estimate turbulent velocities for modeling dispersion. Atmos Environ 42:3833–3841. https://doi.org/10.1016/j.atmosenv.2007.12.061

Venkatram A, Schulte N (2018a) Urban transportation and air pollution. Joe Hayton

Venkatram A, Schulte N (2018b) Modeling Dispersion at City Scale. Urban Transp Air Pollut 139–146. https://doi.org/10.1016/b978-0-12-811506-0.00006-3

Venkatram A, Snyder M, Isakov V, Kimbrough S (2013a) Impact of wind direction on near-road pollutant concentrations. Atmos Environ 80:248–258. https://doi.org/10.1016/j.atmosenv.2013.07.073

Venkatram A, Snyder MG, Heist DK, et al (2013b) Re-formulation of plume spread for near-surface dispersion. Atmos Environ 77:846–855. https://doi.org/10.1016/j.atmosenv.2013.05.073

Yu J, Peng S, Chang J, et al (2018) Inventory of methane emissions from livestock in China from 1980 to 2013. Atmos Environ 184:69–76. https://doi.org/10.1016/j.atmosenv.2018.04.029